

Creating negative illumination for tomographic 3D printing via binary photoinhibition

Bin Wang¹, Weichao Sun², Jadze P. C. Narag³, Hossein S. Mozajin², Thor D. V. Christiansen⁴, Jeppe R. Frisvad⁴, Adrian A. Schiefler⁵, Henning O. Sørensen^{5,6}, Kristoffer Almdal², Aminul Islam¹, Yi Yang^{2,7*}

¹ Department of Mechanical Engineering, Technical University of Denmark; 2800 Kongens Lyngby, Denmark.

² Department of Chemistry, Technical University of Denmark; 2800 Kongens Lyngby, Denmark.

³ Department of Health Technology, Technical University of Denmark; 2800 Kongens Lyngby, Denmark.

⁴ Department of Applied Mathematics and Computer Science, Technical University of Denmark; 2800 Kongens Lyngby, Denmark.

⁵ Department of Physics, Technical University of Denmark; 2800 Kongens Lyngby, Denmark.

⁶ Xnovo Technology ApS, 4600 Køge, Denmark.

⁷ Center for Energy Resources Engineering, Technical University of Denmark; 2800 Kongens Lyngby, Denmark.

* To whom correspondence should be addressed (email: yyan@dtu.dk)

ABSTRACT

Tomographic vat photopolymerization offers high speed, auxiliary-free 3D printing. A fundamental limitation to this emerging technology is the non-negativity constraint, i.e., light engines cannot deliver the information carried by the negative values in a tomogram. We introduce binary photoinhibition, which creates a stationary state with controllable stability for every voxel individually. The information carried by negativities is delivered by a second light engine as external stimuli. We employ the oxygen–lophyl radical pair in free radical polymerization to show that removing the non-negativity constraint increases print accuracy, prolongs process window, accelerates printing and enhances property modulation. The result completes the theoretical framework of reversing tomographic reconstruction for ultrafast 3D printing and enables the direct transfer of knowledge associated with computed tomography to improve print accuracy.

Acronyms

BPS	binary photoinhibitory system
DC	dual color
NEV	negative error voxel
NNC	non-negativity constraint
PEV	positive error voxel
SC	single color
SS	stationary state
TVP	tomographic vat photopolymerization

INTRODUCTION

Computed axial lithography, or tomographic vat photopolymerization (TVP), physically reverses the principle of computed tomography (CT) to realize high-speed, auxiliary-free 3D printing^{1, 2, 3}. In TVP, all points in a 3D object are cured in parallel, and the printing time becomes independent of the number of voxels. TVP eliminates layering-induced defects, produces extremely smooth surface finish and allows the use of highly viscous photoresins. The efficiency and excellent geometric freedom enabled by TVP makes it the focus of emerging volumetric additive manufacturing studies, expanding its applicability to the processing of hydrogel⁴, thermoset^{3, 5}, ceramics⁶ and silica glass⁷. However, a fundamental limitation of TVP is the non-negativity constraint (NNC): while filtering (e.g., using a Ram-Lak filter) in CT introduces negative values to counteract diffuse edges and thereby improve the quality of geometric reconstruction, light engines in TVP cannot deliver negative illumination. As a result, TVP must employ more sophisticated algorithms for sinogram computation^{8, 9} while still settle for a lower print accuracy. Here we show that a binary photoinhibitory system (BPS) creates stationary states (SS) with controllable stability for each voxel individually and can be used to remove the NNC for TVP. BPS can be readily implemented in a dual color tomographic vat photopolymerization (DCTVP) setup (Supplementary Figs. 1-5). Without NNC, we improve the print accuracy, expand the process window, increase the printing speed and enhance the property modulation via greyscale printing.

RESULTS

We propose an ideal BPS that behaves according to

$$\frac{dC_A}{dt} = -k_{0,A,vis} \left(\frac{P_{vis}}{V} \right) \left(\frac{C_A}{C_A + C_B} \right), \quad \text{Eq. 1}$$

$$\frac{dC_B}{dt} = -k_{1,B}C_B + k_{0,B,UV} \left(\frac{P_{UV}}{V} \right) - k_{0,B,vis} \left(\frac{P_{vis}}{V} \right) \left(\frac{C_B}{C_A + C_B} \right), \quad \text{Eq. 2}$$

in which C is concentration (mol m^{-3}), t is time (s), k_0 and k_1 are zeroth (mol J^{-1}) and first (s^{-1}) order rate constants, P is power of irradiation (mW) and V is voxel volume (m^3). Subscripts vis and UV denote the type of irradiation while A and B denote the species that introduce nonlinear photoresponse. Species A pre-exists and is stable without illumination (e.g., oxygen in free radical polymerization). B is a transient species that

- i) can be generated via external stimulus (e.g., UV illumination),
- ii) competes with A for the incident light that initiates photopolymerization,
- iii) is stable in the absence of external stimulus, and
- iv) inhibits polymerization.

Species B redefines system behavior. Without B , single color (SC) TVP operates unidirectionally along the axis of abscissas (Fig. 1a). A voxel always starts at $(C_{A0}, 0)$, and illumination pushes the state of the voxel towards the origin $(0,0)$, where polymerization occurs. If two voxels were adjacent and we aim to cure one but not the other, we need to build a dose contrast so that the illumination could be terminated when the dose received by the former surpasses the curing threshold while that received by the latter does not. We let the term “process window” denote the period of time that meets this requirement. Unfortunately, the entire curing volume in TVP is illuminated from various angles, and voxels inevitably receive irradiation meant for the voxels that they shadow. Ultimately, all voxels move towards the origin – the only SS for SCTVP.

Introducing species B creates a new SS on the axis of ordinates

$$(C_A, C_B)_{SS} = \left(0, \frac{k_{0,B,UV}}{k_{1,B}} \frac{P_{UV}}{V} - \frac{k_{0,B,vis}}{k_{1,B}} \frac{P_{vis}}{V} \right). \quad \text{Eq. 3}$$

The sinogram computation becomes an exercise of designing the transient profiles of $P_{vis}(t)$ and $P_{UV}(t)$ such that the states of all polymerizing voxels move rapidly towards the origin, while those of non-polymerizing voxels move slowly towards an alternative SS. The SS can be defined individually for each voxel (Fig. 1b-c, Supplementary Movie 1). Near an SS, the system is governed by

$$\frac{dC_A}{dt} \Big|_{SS} = -\frac{k_{0,A,vis} k_{1,B} P_{vis}}{k_{0,B,UV} P_{UV} - k_{0,B,vis} P_{vis}} C_A, \quad \text{Eq. 4}$$

$$\frac{dC_B}{dt} \Big|_{SS} = \frac{k_{0,B,vis} k_{1,B} P_{vis}}{k_{0,B,UV} P_{UV} - k_{0,B,vis} P_{vis}} C_A - k_{1,B} C_B + k_{0,B,UV} \left(\frac{P_{UV}}{V} \right) - k_{0,B,vis} \left(\frac{P_{vis}}{V} \right), \quad \text{Eq. 5}$$

of which the eigenvalues are

$$\lambda_1 = -\frac{k_{0,A,vis} k_{1,B} P_{vis}}{k_{0,B,UV} P_{UV} - k_{0,B,vis} P_{vis}}, \quad \text{Eq. 6}$$

$$\lambda_2 = -k_{1,B}. \quad \text{Eq. 7}$$

Both eigenvalues scale with $k_{1,B}$, suggesting that a system moves quickly towards an SS if B has a short half-life; large $k_{1,B}$ reduces the ordinate, bringing it closer to the origin and thus dragging all voxels indifferently towards polymerization. Therefore, in contrast to previous applications¹⁰, photoinhibitors with a short lifespan are not favored in TVP. Moreover, the SS can be swapped between a stable and a saddle point at any time by adjusting the relative output of the two light engines (P_{UV} and P_{vis}). If we could direct solid voxels towards the origin and steer non-polymerizing voxels away by controlling $P_{UV}(t)$, it becomes feasible to expand the process window indefinitely even though P_{vis} remains positive for all voxels (Supplementary Movie 2-4). If the state of a system is denoted by \mathbf{r} (Fig. 1a, yellow vector), the effect of P_{UV} is to lift \mathbf{r} upwards and P_{vis} to push it leftwards. It is thus possible to pair P_{UV} and P_{vis} to create an acceleration pointing away from the origin (the only polymerization

point), i.e., $\mathbf{r} \cdot \mathbf{r}' = 0$. If so, P_{UV} and P_{vis} are effectively the negative of each other because the system revolves counterclockwise around the origin and sustained illuminations do not move it any closer or farther away from the origin. The NNC is thus removed by substituting the negative values in a sinogram with positive illumination of a different wavelength as the external stimuli for Species B.

Inspired by the work of T.F. Scott's group ¹¹ (Supplementary Figs. 6-12), we discovered that the oxygen–lophyl radical pair reasonably approximates the behavior of the A-B pair of an ideal BPS in free radical polymerization (Fig. 1d-f, 1h-i, Supplementary Figs. 13-14), and we used this exemplary pair and constructed an apparatus DCTVP (Fig. 1g) to demonstrate a TVP system without NNC. We first show that photochemical negativity introduced via a BPS 1) improves printing accuracy and 2) significantly prolongs the process window. With NNC, negative values are either set to zero, or eliminated during iterative computation. The former leads to loss of information and thus a reduced print accuracy, whereas the latter leads to a distorted histogram and susceptibility to over-exposure. We printed cuboids with a 7.2 x 7.2 mm² cross section and numerically simulated the process to understand these impacts of NNC (Fig. 2a-e, Supplementary Movies 5-7). The goal is to minimize the number of error voxels, which are either intended solid voxels that do not receive sufficient light dose and thus remain unpolymerized (negative error voxels, or NEVs) or voxels that should have remained unpolymerized but are over-dosed to solidify (PEVs). With NNC, the printing time is determined by the minimum number of full rotations required to eliminate NEVs, and print quality declines with increasing number of PEVs generated during these rotations. Setting negativities to zero (Supplementary Fig. 16, SC-1) amounts to purposely turning voxels most susceptible to over-exposure (e.g., corners of the square) into PEVs, and thus limiting the achievable print accuracy. Yet, if the NNC is accounted for during iterative sinogram computation (SC-2), the extra doses for most susceptible voxels are dispensed among the

entire curing volume, i.e., the high tendency of a few voxels to become PEVs is reduced at the expense of tolerating undesired dose build-up in many other voxels. As a result, thus calculated projections offer high accuracy, but the print quality declines quickly due to the soaring of PEVs once the optimal termination point is missed. Removing the NNC significantly prolongs the process window without compromising accuracy. We divided the original sinogram into two parts according to the signs of pixel intensity. The positive pixels were projected by the visible source and the negative ones by UV. The information carried by the negativities was thus preserved by taking the absolute value of corresponding pixels, converting them to positive, greyscale UV patterns. As UV stabilizes voxels at an unpolymerized SS, the increase of PEVs can be arrested after all NEVs are eliminated. Before NEVs disappear completely, the shape of a workpiece was sensitive to the rotation period (Fig. 2e). With a rotation period of 24 s this sensitivity persisted for the first three full rotations in our tests. With NNC, SC mode could not prevent over-exposure at the four corners. Without NNC, DCTVP not only produced more accurate workpieces, but managed to keep improving print quality after three full rotations. The delay in maximizing accuracy was also consistent with the model prediction and was attributable to the excessive radical scavengers generated during NEV elimination.

The evolution of the Jaccard index suggests that the printing can be divided into three phases: induction, where no polymerization occurs; under-exposure, where NEVs are quickly eliminated; and over-exposure, where increasing PEVs deteriorates print quality. During induction, radical scavengers are selectively removed. With NNC, induction is essential for establishing sufficient dose contrast so that the workpiece is less susceptible to over-exposure. Toombs et al.⁷ showed that prolonging the inductive period by increasing pre-dissolved radical scavenger prevents unintended polymerization and improves negative features. If the NNC is lifted, however, dose contrast can be established during

polymerization. We reduced pre-dissolved oxygen by flushing the resin with white light for 16 s (Fig. 2f). When we printed a cuboid after such pre-processing in dual color (DC) mode, workpiece appeared after 12 s of co-illumination, followed by an additional 17 s of solidification. When the pre-processed resin was used in the SC mode, illumination led immediately to intractable polymerization and a sharp increase in PEVs. Even with *in situ* imaging we could not determine when to stop the illumination without causing severe over-exposure. Overall, by shortening the inductive period, we managed to cut the printing time from 72 s to 29 s and still achieved superior print quality in the cuboid tests.

Greyscale printing generates property contrast within a workpiece by delivering varied light doses to different voxels. A main challenge to grayscale tomographic printing is the lack of orthogonality between geometry control and property modulation. Using stiffness control as an example – if we want to print a heart shape, with the left half softer than the right, NNC limits the achievable contrast because the voxels at the vicinity of the stiffer half are particularly susceptible to unintended polymerization, i.e., the part can only be stiffened at the expense of increasing nearby PEVs. Moreover, the softer half keeps receiving undesired irradiation after polymerization initiates. Its extent of polymerization, which can be sensitive to small increases in incident dose (Fig. 1d-f), keeps rising until the illumination ends, thus limiting the achievable softness. In addition, sinogram computation with NNC requires a heuristic threshold that represents a tolerable level of unintended energy build-up³. This threshold also sets the lower limit for pre-definable property contrast. Introducing the BPS helps address this challenge in two ways. Before polymerization, the effect of BPS is subtractive – it erases undesired energy build-up and reverses the status of a voxel along the nonlinear response (Supplementary Fig. 17). After polymerization, BPS enables photomasking – the UV illumination arrests monomer conversion and prevents undesired hardening (Supplementary Fig. 16c, Supplementary Movie 8). The subtractive effect is

clearly manifested by the expansion of the process window, which allows sustained dose delivery without causing over-exposure nearby and thus increases the upper bound of pre-definable property contrast. To show that the BPS arrests undesired stiffening after polymerization, we printed the two-halves heart using both modes. The pre-defined dose per rotation for the left part was 50% of that of the right part and we stopped the illumination immediately after workpiece formation (46 s for SC and 48 s for DC). The quality of the DC samples appeared superior as the cleavage above the joint of the two mechanically differentiated halves was well preserved (Fig. 2g). In contrast, the cleavage was partially filled in SC mode even with shorter exposure (Fig. 2h). Compression tests showed that UV arrested the degree of polymerization, producing significantly softer parts (0.68 MPa w/ DC vs 1.43 MPa w/ SC, Fig. 2i) yet still created a 270% property contrast.

DISCUSSION

We measured the absorbance of M-1 resin using UV-Vis spectroscopy, and UV illumination at 70 mW/cm² for 15 seconds did not deplete the *o*-Cl-HABI (Fig. 3a). Also, lophyl recombination did not follow a first order law and therefore did not have a constant half-life. However, its decay is sufficiently slow to be cumulative during printing. The generation of lophyl does follow a zeroth order kinetic regarding UV illumination and upscales with the power of irradiance (Fig. 3b). It remains unclear how the competition between oxygen and lophyl for visible light scales with their relative concentration ($RC = [\text{Oxygen}] / [\text{Lophyl}]$). However, the prolonged induction period due to lophyl's presence varied according to the timing of introducing UV (Fig. 3c-f). When 30 seconds of UV illumination was introduced before visible light, the induction period was prolonged from 30 s to 38 s (Fig. 3d). When the same UV illumination was introduced after 30 seconds of visible light illumination, the induction period was instead prolonged to 50 s (Fig. 3e). The latter represents a case with a

relatively lower RC, and the extended induction indicates that the consumption of visible dose by lophyl radicals does correlate positively with its relative concentration to oxygen – in the second case, more lophyl was consumed at a low RC and thus less was lost to self-recombination. Co-illumination of both sources was employed to minimize the effect of self-recombination, and the inductive period was further prolonged to 68 s (Fig. 3f).

We propose a simple BPS scheme for TVP which allows the use of external stimuli to create SS for each voxel individually and to swap the stability in real time. Such freedom of navigating the phase diagram grants us the power to lift the NNC, a fundamental constraint in TVP. Species B in Eqs 1-2 represents an idealization and we here underscore the nonideality of lophyl radical (Fig. 3a-b, Supplementary Note and Figs. 18-23). Each bis[2-(*o*-chlorophenyl)-4,5-diphenylimidazole] (*o*-Cl-HABI) generates two lophyl radicals upon photolysis, and the capacity of creating photochemical negativity scales with its concentration ($[o\text{-Cl-HABI}]$) stoichiometrically. *o*-Cl-HABI also causes strong light extinction in photoresin. If we define W as the equivalence between UV and visible irradiation (Supplementary Eq. 8), increasing $[o\text{-Cl-HABI}]$ would increase achievable W , expand the process window and enhance pre-definable contrast, but at the cost of increased W variance across the curing volume. The latter, not accounted for during sinogram computation, compromises print accuracy. Lophyl radicals self-recombine and disappear spontaneously. A shorter lifespan entails greater energy consumption to reach the same W . Also, the self-recombination reduces effective W in a way that depends on the illumination history (Fig. 3c-f), which complicates experimental trial-and-error. Then again, the limited lifespan can be advantageous in countering the undesired UV build-up in voxels that are meant to polymerize. Overall, perhaps the most important implication of removing NNC is that the entire library of knowledge for optimizing CT reconstruction via introducing negativity to

sinograms may now become transferrable to TVP research, to improve the quality of ultrafast 3D printing.

METHODS

Materials

The methacrylate based photoresin was prepared by mixing triethylene glycol dimethacrylate (TEGDMA, CAS#109-16-0, Sigma–Aldrich) and bisphenol A glycerolate dimethacrylate (bisGMA, CAS#1565-94-2, Sigma–Aldrich) at a weight ratio of 1:1, adding 0.2 wt% camphorquinone (CQ, CAS# 10373-78-1, ≥96.5% purity, Sigma–Aldrich) and 0.5 wt% ethyl 4-dimethylaminobenzoate (EDAB, CAS# 10287-53-3, Sigma–Aldrich) as the photoinitiator and co-initiator, respectively. 2,2'-Bis(2chlorophenyl)-4,4',5,5'-tetraphenyl-1,2'-biimidazole (*o*-Cl-HABI, CAS# 7189-82-4, TCI Europe) was first dissolved in tetrahydrofuran (THF, CAS# 109-99-9, Fisher Scientific) at 28 wt% then added to the photoresins at 1 wt% (M-1), and 3 wt% (M-3) concentrations. An alternative resin was prepared by mixing bisphenol A glycerolate diacrylate (BPAGDA, CAS# 4687-94-9) and poly(ethylene glycol) diacrylate (PEGDA, CAS# 26570-48-9, average Mn 250 w/100 ppm 4-methoxyphenol as inhibitor) in the weight ratio of 1:1, incorporating 0.1 wt% CQ and 0.25 wt% EDAB as the initiator and co-initiator respectively. *o*-Cl-HABI solution (28 wt% *o*-Cl-HABI: 72 wt% THF) was then added to the mixture at varied weight ratios. All the chemicals were obtained and used as received without further purification.

DCTVP assembly

The dual-color tomographic vat photopolymerization (DCTVP) assembly was described previously³ and is illustrated in Supplementary Fig. 1 (optomechanical parts are tabulated in Supplementary Table 1). The UV and visible light paths were built orthogonally and the illumination for *in situ* imaging was merged into the visible light path via a dichroic mirror

(DMSP490L Thorlabs, 490 nm Cutoff), which let through visible light under 490 nm from S1 and reflected longer wavelengths from S3.

Component S1 is a DLP projector (XD1270D, Acer, Acer Denmark), used with an optical lens ($f = 200$ mm) to project visible light into the curing volume. Illumination from a UV DMD projector (S2, VISITECH-LRS-4KA, Visitech, Norway) is focused through a 4f-lens system (L2: $f = 200$ mm & L3: $f = 300$ mm), on the Fourier plane of which an aperture was used to block unwanted diffraction orders from the DMD and to improve intensity homogeneity. Two projecting centerlines were aligned to intersect at the rotation axis of the curing volume. *In situ* imaging was illuminated by a collimated LED source (S3, $\lambda = 625$ nm, M625L4-C4, Thorlabs) through two 4f lens systems. The first (L4: $f = 50$ mm & L5: $f = 200$ mm) was used to focus the beam into the central plane of the curing volume, and the second (L6: $f = 200$ mm & L7: $f = 50$ mm) to demagnify the curing volume to the imaging size of the detector (CMOS camera, MQ042CG-CM, XIMEA). LP represents the long-pass filter (610 nm long pass), used to block light from S1 so that the camera detected illumination only from S3. The maximal projection area was 12.3×22 mm². A cylindrical test tube ($\varnothing 12.4$ mm) containing photoresin was mounted to a motorized rotation stage (PRM1/MZ8, Thorlabs) located at the intersection of the two light paths. A cuboid vat containing index-matching fluid was placed outside the test tube, with walls perpendicular to incident beams.

Optical specifications

A voxel in TVP is a fan-shaped cube and has two characteristic lengths ³. The pixel sizes, obtained from the dimensions of the projection field divided by number of pixels, were 8.1 μm for UV and 118 μm for visible light. The edge length of the fan in this study was 21.6 μm when tubes of 6.2 mm radius and 1800 frames per rotation were used.

We used a modulation transfer function (MTF) to quantify the capability of our optical system to preserve the details of an input image. This is defined by

$$MTF = \frac{m_{output}}{m_{input}}, \quad \text{Eq. 8}$$

where m is the intensity contrast of an image

$$m = \frac{I_{\max} - I_{\min}}{I_{\max} + I_{\min}}, \quad \text{Eq. 9}$$

and I_{\max} and I_{\min} are the maximum and minimum light intensity values of a contrast line pair.

In this study, the MTF was measured as a function of spatial frequency ν , which is varied by changing the number of alternating black and white line pairs (Supplementary Table 2).

The MTF was measured for three planes: the focal plane, and two planes located on both sides of and 6.2 mm away from the focal plane. In each plane, we measured the MTF at three different positions: (0, 0), (3.1, 5.5) and (6.2, 11), where (0, 0) is the center of the plane in question. A CMOS camera (MQ042CG-CM, XIMEA) was used to record the output image.

The pixel size of the camera was 5.5 μm . The captured images were then processed with *Image J* to get the light intensity values. Supplementary Figs. 2-3 show the results. The MTF of UV and visible light projections decreased to 0.2 and 0.4, respectively, when the corresponding line pair frequency reaches 8.8 and 5.2. The effective pixel pitch thus calculated were 58 μm for UV and 118 μm for visible light.

Fourier transform infrared spectroscopy

Attenuated total reflectance - Fourier transform infrared spectroscopy (ATR-FTIR) was used to measure double bond conversion (Spectrum 100, PerkinElmer, UK). A 1.5 mm ring was used as sample holder, placed next to the ATR cell of the spectrophotometer. A pipette was used to control the sample volume and transfer the test subjects. The spectra were obtained

from 4000 cm⁻¹ to 650 cm⁻¹ with one scan per 8.3 or 4.3 seconds. Real time conversion was calculated by monitoring the C=C alkene stretch peak at 1638 cm⁻¹ and that of the aromatic ring at 1610 cm⁻¹.

During *in situ* measurements, a sample was illuminated using 470 nm blue LED (SOLIS-470C, Thorlabs) and/or 365 nm UV light (M365LP1-C1, Thorlabs). The output power of the LEDs was set via LED drivers, and irradiance was measured prior to each experiment using a standard photodiode power sensor (S120VC, Thorlabs) working in the 200 - 1100 nm wavelength range and recorded with an optical power console (PM400, Thorlabs).

UV-Vis spectroscopy

UV-Vis spectroscopy was performed with an Agilent Instrument Exchanges Service Model G1103A using a 10 mm path length quartz cuvette to measure the absorption character of the chemical reagents. *o*-Cl-HABI and CQ were dissolved in THF and diethylene glycol dimethyl ether (DGDE, CAS# 111-96-6), respectively, at varied concentrations (Supplementary Figs. 6-8). The absorbance spectra were collected from 200 nm to 900 nm. As a reference, the absorption characteristics of the solvents were also measured. The extinction coefficient \mathcal{E} of the reagents was calculated using the Beer-Lambert law

$$A = -\log_{10} \frac{I_t}{I_0} = \varepsilon \ell c, \quad \text{Eq. 10}$$

of which,

ε – extinction coefficient (L/cm/g or L/cm/mol)

ℓ – cuvette path length (10 mm)

c – regent concentration (g/L or mol/L)

In situ UV-Vis measurement was used to evaluate the evolution of the lophyl radical concentration upon the photolysis of *o*-Cl-HABI. Resin M-1 and 10 mm path disposable

cuvettes were used. In each test, UV and visible sources were placed on the opposite sides of the cuvette. In order to remove pre-dissolved oxygen molecules, each sample was first illuminated by visible light for 15 s at 5 mW/cm², then by UV for 20 s (Fig. 3a-b). The *in situ* absorbance was recorded every 6.9 s. All measurements were carried out in a dark environment.

Mechanical characterization

Compressive tests were conducted using a Texture Analyzer (Stable Micro Systems, Godalming, UK). A cylindrical metal probe (Ø2 mm) was used with an advancing speed of 0.1 mm/s. The compressive stress was recorded as a function of strain, from which the corresponding elastic modulus was extracted.

Post processing

Isopropanol was used to rinse off residual resin attached to the workpiece after printing. Additional postprocessing, when sample hardening was needed (not in greyscale printing), was conducted by heating a sample to 60 degree and exposing it to 405 nm UV for 2 h using the Form Cure automate postprocessing machine (FH-CU-01, Formlabs, USA).

Other characterization methods

Before we received the 3Shape E4 laboratory scanner, we used a few other methods to evaluate the geometry of early printouts. Scanning electron microscope (SEM) imaging was carried out using an AFEG 250 Analytical ESEM (Oxford instruments). The sample was coated with a 5 nm thick layer of gold using a Quorum coater (Q150T es) before each analysis. X-ray microtomography (μ CT) was conducted using a Zeiss Xradia 420 Versa instrument at the 3D Imaging Center, DTU (Carl Zeiss X-ray Microscopy, Inc., Pleasanton, USA). The tungsten X-ray source was operated at 40 kV (unfiltered) and a current of 250 μ A. 801 radiographs were recorded while rotating the sample 180° with an exposure time of 1.5 s

by a CCD detector (at an effective pixel size $14.66 \mu\text{m}$, 1024×1024 pixels binned 2 by 2 from a 2048^2 detector). The 3D image of the sample was reconstructed from the radiographs using the Feldkamp-Davis-Kress (FDK) filtered back projection method ¹² as implemented in the software by the vendor. The SEM and μCT results served as a cross-checking for the scanning results using the 3Shape scanner and are not included in the main text.

Geometry characterization

Printouts were coated with a thin layer of white spray (AESUB, Germany) and scanned using a 3Shape E4 laboratory scanner (3Shape, Denmark). Each scan generated an STL file that could be compared with the original STL design to calculate a Jaccard index using

$$J(\text{Design}, \text{Workpiece}) = \frac{\text{Design} \cap \text{Workpiece}}{\text{Design} \cup \text{Workpiece}} . \quad \text{Eq. 11}$$

In Eq. 11, $\text{Design} \cap \text{Workpiece}$ is the intersection of the volume of the 3D scanned printout (hereafter just workpiece) and the volume of the original STL design (hereafter just design). $\text{Design} \cup \text{Workpiece}$ is the union of the volumes of the design and the workpiece. In case of complete similarity, where the intersecting volume is equal to the volume of both the design and the workpiece, the Jaccard index is 1. In case of no overlapping volume, the Jaccard index is 0. The intersection of the volumes of the design and the workpiece is computed by aligning the two and then finding the overlapping volume. To do so, the original design is first mirrored in the YZ-plane, as the rotation direction during the printing process changes the chirality of the workpiece ³. Second, the design is re-scaled to match the scale of the workpiece. Finally, the design is aligned with the workpiece by using a rigid-body transformation. After these steps, the overlapping volume can be computed. The process of mirroring, re-scaling and aligning the design with the workpiece to find the volume of both and the overlapping volume for the Jaccard index computation is described in Algorithm 1

below. The geometry processing library PyGEL (<https://github.com/janba/GEL>) is used to create the meshes from the polygonal faces in the STL files, remove the print support from the workpiece, compute Garland- Heckbert simplifications to reduce the computational cost ¹³, obtain the skeletons (sparse representations of the meshes) using local separators ¹⁴ in order to make a coarse alignment, close the holes in the workpiece that were artifacts from the scanning process, triangulate the closed holes in the workpiece and compute the volume of the design and the volume of the workpiece ¹⁵. The geometry processing library libigl (<https://libigl.github.io/>) is used to load the polygonal faces from the STL files. It is also used to compute the Generalized Winding Number ¹⁶ at each of the sampled points within the bounding box to determine if each point is inside both meshes. With this, the volume intersection between the design mesh and the workpiece mesh can be approximated.

Algorithm 1 Computation of Jaccard index between original STL design and STL file of 3D scanned printout

- 1: **Input:** An STL file of the workpiece, an STL file of the laboratory scanner sample holder, an STL file of the original design.
- 2: For each STL file, use a geometry processing library to load the polygonal faces and stitch these together to form a mesh.
- 3: Remove the sample holder from the workpiece mesh using the mesh from the holder.
- 4: Center each of the meshes around the origin by subtracting the respective means of the mesh vertex positions.
- 5: Mirror the design mesh in the YZ-plane.
- 6: Compute the bounding box of the workpiece mesh and the bounding box of the design mesh.
- 7: Find the dimensions of the bounding boxes and rescale the design mesh to the scale of the workpiece mesh.
- 8: Simplify the two meshes using the Garland-Heckbert method ¹³ so the meshes contain a maximum of 10,000 triangle faces.
- 9: Obtain the skeletons of the simplified design mesh and the simplified workpiece mesh using local separators ¹⁴.
- 10: Do a coarse alignment of the design mesh to the workpiece mesh using the Iterative Closest Point (ICP) algorithm ¹⁷ on the skeletons of the design mesh and the workpiece mesh until a maximum of 1000 iterations is reached or until the nearest point neighbors in the skeleton of the design mesh do not change from iteration k to iteration $k + 1$.
- 11: Do a new alignment of the design mesh to the workpiece mesh using the ICP algorithm.
- 12: Close holes in the workpiece mesh and triangulate the closed holes.
- 13: Find the bounding box of both the design mesh and the workpiece mesh.
- 14: Sample equidistant points within the bounding box of the design mesh and the workpiece mesh using a pre-determined resolution of 1 mm³.
- 15: Compute the Generalized Winding Number ¹⁶ at each of the equidistant sampled points within the bounding box for both the design mesh and the workpiece mesh.

- 16: Obtain the intersection volume (V_i) of the design mesh and the workpiece mesh by computing the number of point samples within the design mesh and the workpiece mesh.
- 17: Compute the volume delimited by the design mesh (V_d).
- 18: Compute the volume delimited by the workpiece mesh (V_w).
- 19: Compute the Jaccard index (J) based on the volume measurements:
$$J = \frac{V_i}{V_d + V_w - V_i}$$

Resin response calibration

Irradiance was measured as a function of greyscale intensity for both sources (Supplementary Figs. 4-5). Ball series at the rotation center were then printed at various UV intensities for photoresponse calibration (Supplementary Fig. 14). Six filled circles ($\varnothing 3$ mm) were projected by S1 at maximum intensity (grayscale 255) and by S2 at incremental intensities from 0 to 255. Rotation period was 24 s. The delay in the appearance of workpieces reflected the efficiency of negativity generation as a function of UV irradiance. This information was used to aid experimental trial-and-error and to calibrate numerical simulations.

Imbued dose calculation

The estimate of light doses used in each print follows our previous paper³. The grayscale intensities in each pattern series were first correlated to the irradiance (Supplementary Fig. 4) and then summed up according to the exposure time. Results are compiled in Supplementary Table 3.

Sinogram computation

We employed two sinogram computation methods in this study – volumetric ray casting for quick screening of STL files of interest, and an iterative method inherited from our previous study³ for the printing results presented in the main text. In volumetric ray casting, the corresponding projection image (slice of the sinogram) at each projection angle θ was generated by using a ray tracer to cast a ray through the volume of the design (a triangle mesh obtained from the STL file) for each pixel in the projection image (Supplementary Fig. 15). Consequently, a ray parameterized as a straight-line shots through the position of the i 'th

pixel in the image. This acts as the starting position, \mathbf{e}_i , of the ray, going in the direction of the unit vector, \mathbf{v} , which is orthogonal to the plane of the projection image. The grayscale color of a given pixel in the projection image was then determined by the intensity of the ray cast through the volume and starting from that specific pixel. This intensity was determined by reversing the law of exponential attenuation:

$$I(d) = 1 - \exp(-\sigma d), \quad \text{Eq. 12}$$

where d is the distance the ray travels through the volume of the design, σ is an attenuation coefficient, which depends on the material and the printing time, and $I(d) \in [0, 1]$ is the intensity of the ray, which has passed a distance d through the volume of the design. If a ray does not pass through the volume of the design, the output intensity is $I(0) = 0$ and the pixel, which the ray was cast from, is colored with the RGB color $(0, 0, 0)$. The grayscale color of a pixel, where the ray passed a distance d_k through the volume, is $255 \cdot (I(d_k), I(d_k), I(d_k))$. In the experimental setup, a lens is used to collimate the light from Projector S1. Rays therefore start within a pixel area and go in the direction orthogonal to the image plane. An average of multiple ray samples with random starting positions were used within each pixel area to avoid aliasing (staircase artifacts) along edges in the projection images.

To mitigate the effect of sharp edges being smeared out on the printout during the printing process, the intensities of rays passing through sharp edges were adjusted. To detect the sharp edges in the design, the connectivity information of the triangle mesh of the design (knowledge of a triangle face's neighboring triangle faces) was used to find the size of the dihedral angles (the angle between two neighboring triangle faces) of all the edges in the triangle mesh. When a ray passed through an edge with a dihedral angle greater than or equal to 90 degrees, the intensity of that ray was adjusted. Consequently, the intensities were set to $I = 1$, so the color of the corresponding pixels in the projection image were $(255, 255, 255)$.

For each printout, $\sigma = 4.25$ and 1200 projection images of resolution 1024×768 (width \times height) per rotation were generated using volumetric ray casting. A rotation period of 24 seconds was used. In order to print the design, a movie in AVI-format with a frame rate of 50 Hz was generated from the projection images and then displayed by the projector S1. These parameters were chosen based on empirical tests. Volumetric ray casting does not require STL slicing, does not create any negativity in a sinogram and the computation can be accelerated by graphical processing units. Also, patterns generated using volumetric ray casting are free from aliasing artifacts.

Iterative sinogram computation follows our previous methodology ³. An STL file was sliced using ChiTuBox (CBD-Tech, SZX) and the grey values of the pixels in the resulting TIFF stack were adjusted in accordance with desired target dose distribution. The initial sinogram was computed using naïve forward projection, i.e. for each projecting angle θ , the position $D(d)$ of the projection of point $P(x,y)$ on a 1D detector was determined by

$$d = y \cos \theta - x \sin \theta, \quad \text{Eq. 13}$$

and the grey value of P was added to the light intensity at D . The initial sinogram thus generated was back-projected to estimate reconstruction quality. We used a logistic equation to simulate the nonlinear response of free radical polymerization to energy build-up. The critical incident dose was estimated according to tests presented in Supplementary Fig. 14. The workpiece was then compared with the original design and the difference was forward projected to generate a correction for the previous sinogram. The correction may result in negativities. If these negativities are kept until the last iteration and then set to zero, we have SC-1 (Supplementary Fig. 16B). If they are set to zero in each iteration, we have SC-2. If the negativities are left untreated, the resulting sinogram can be divided according to the signs and be used directly in a dual color, binary photoinhibitory system, and we have DC in

Supplementary Fig. 16C. When using SC-2, we observed that the negativity removal prevented the sinogram from fully reconstructing the desired geometry, and thus the heuristic thresholding became essential in generating sinograms for satisfactory print quality. In contrast to volumetric ray casting, computational time required for this iterative method scales with the number of slices in the axial direction and is therefore less favorable for quick STL tests.

Numerical simulation

Simulation of printing process follows our previous numerical scheme ³. The curing volume was discretized using the same voxelization scheme in sinogram computation and the reactive transport of oxygen (A), lophyl radical (B) and *o*-Cl-HABI (C) was analyzed by solving

$$\frac{dc}{dt} = \nabla^2 c + Da \quad . \quad \text{Eq. 14}$$

Using oxygen as an example, c is the dimensionless inhibitor concentration:

$$c = \frac{C_{A0} - C_A}{C_{A0}}, \quad \text{Eq. 15}$$

where C_A and C_{A0} are the concentration and the initial concentration of oxygen in the polymer precursors, respectively (mol/L). Da is the Damköhler number:

$$Da = l^2 \frac{k_0 \int_{\lambda} \alpha(\lambda) I(\lambda) d\lambda}{C_{A0} D_A}, \quad \text{Eq. 16}$$

where l is voxel size (m), D_A the diffusivity of inhibitor (m²/s), α the absorption coefficient and I the irradiance (mW) of wavelength λ (nm), k_0 is the zeroth order rate constant that relates inhibitor consumption to irradiation. Da evolves spatiotemporally as a consequence of changing irradiation angle and nonlinear polymer response. The Fickian fluxes N_A for each voxel were computed at the six inter-voxel surfaces and photochemical reactions were treated

as a zeroth order sink for oxygen, first order sink for *o*-Cl-HABI and second order sink for lophyl radicals, i.e.

$$r_A = -k_{0,A,vis} P_{vis} \left(\frac{C_A}{C_A + C_B} \right), \quad \text{Eq. 17}$$

$$r_B = -k_{0,B,vis} P_{vis} \left(\frac{C_B}{C_A + C_B} \right) - k_{2,B} C_B^2 + k_{1,C,UV} P_{UV} C_C, \quad \text{Eq. 18}$$

$$r_C = k_{2,B} C_B^2 - k_{1,C,UV} P_{UV} C_C. \quad \text{Eq. 19}$$

It was necessary to treat the photolysis of *o*-Cl-HABI as first order to account for the limited capacity of lophyl radical generation. Concentration was assumed uniform inside each voxel. Reactive transport was simulated to assist experimental trial-and-errors for determining optimal exposure time to operate TVP in the dual-color mode. Simulation was not part of the iterative sinogram computation. Supplementary Movies 2-5 were results of numerical simulations.

Figure 1

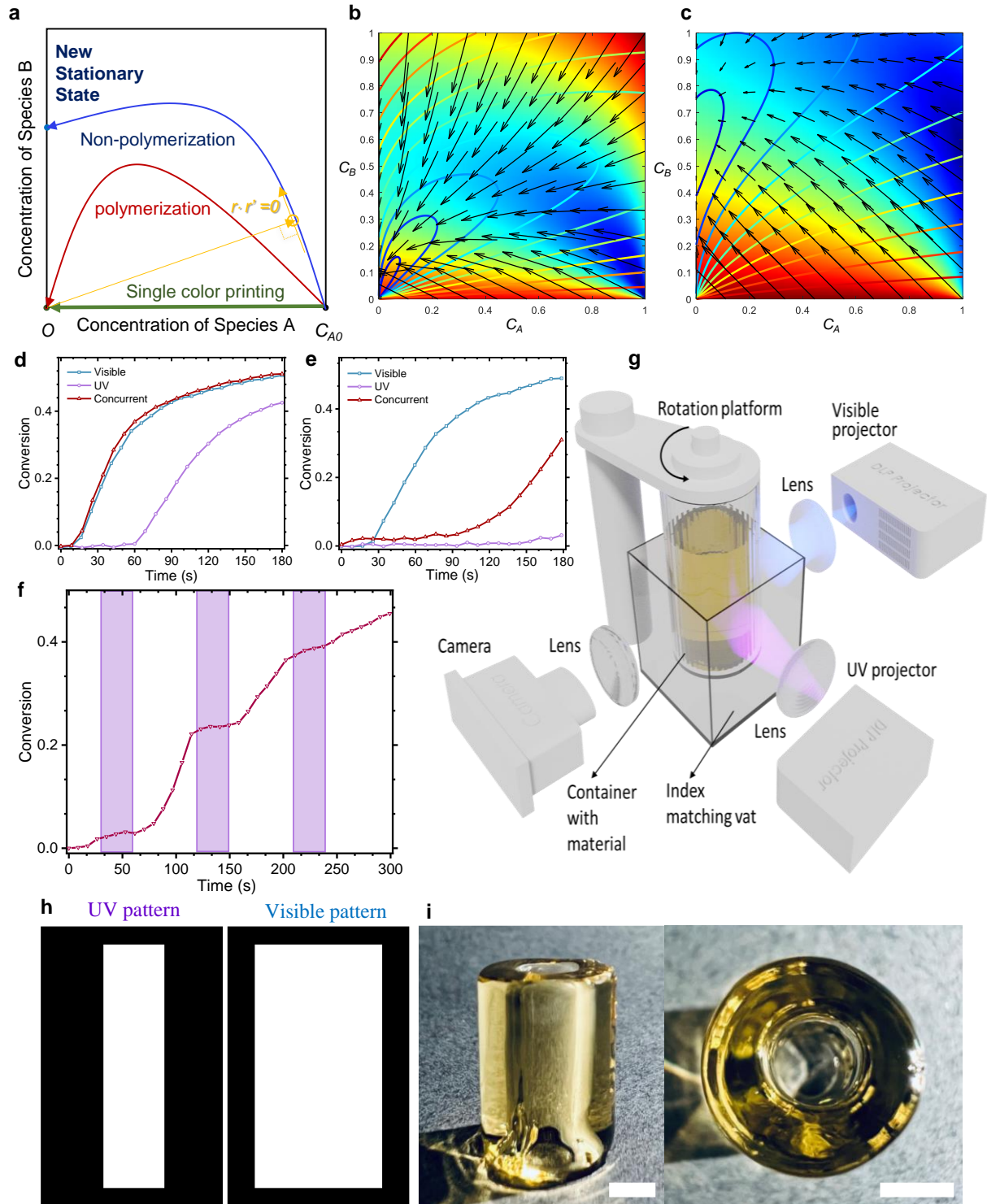


Figure 2

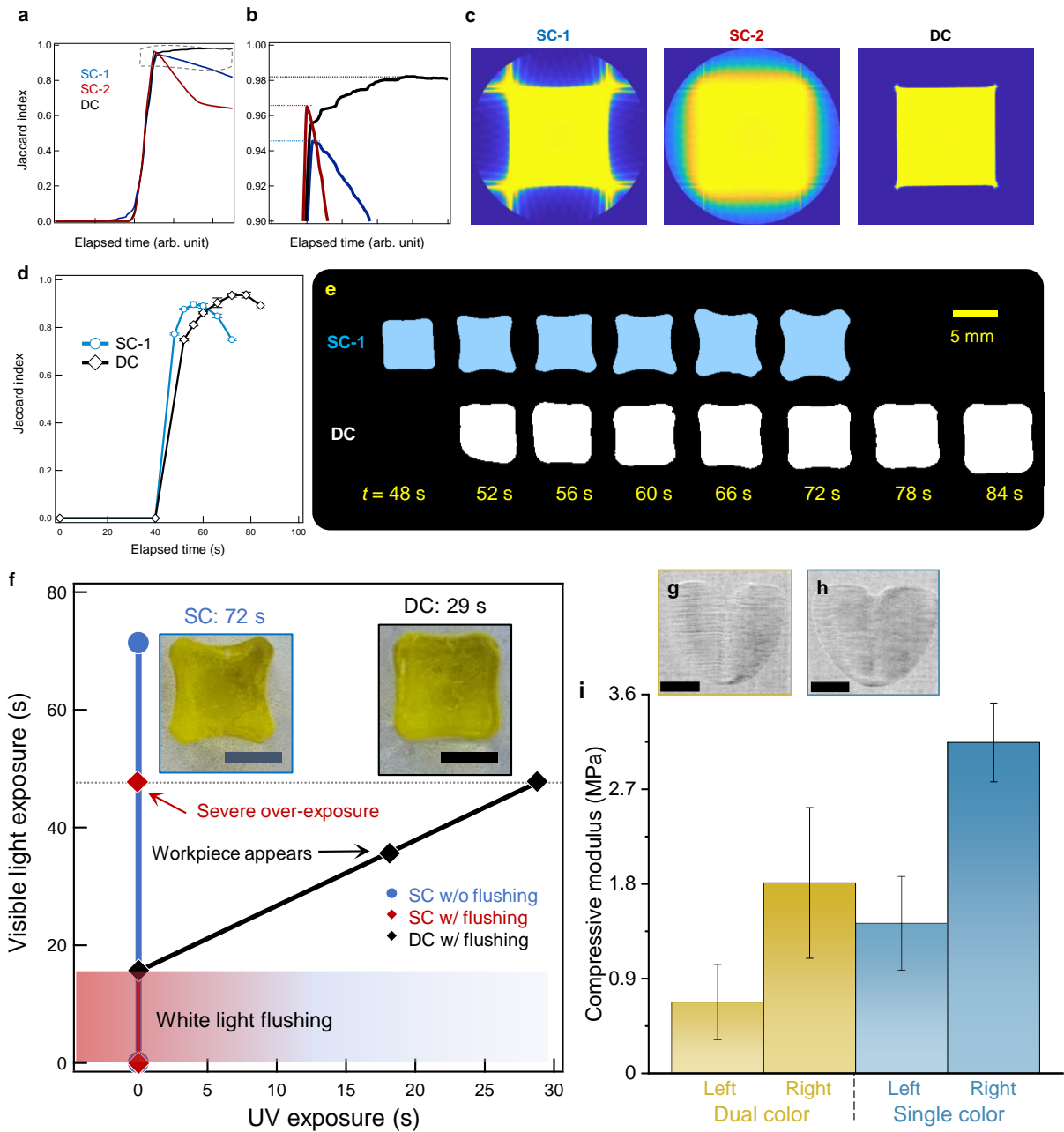


Figure 3

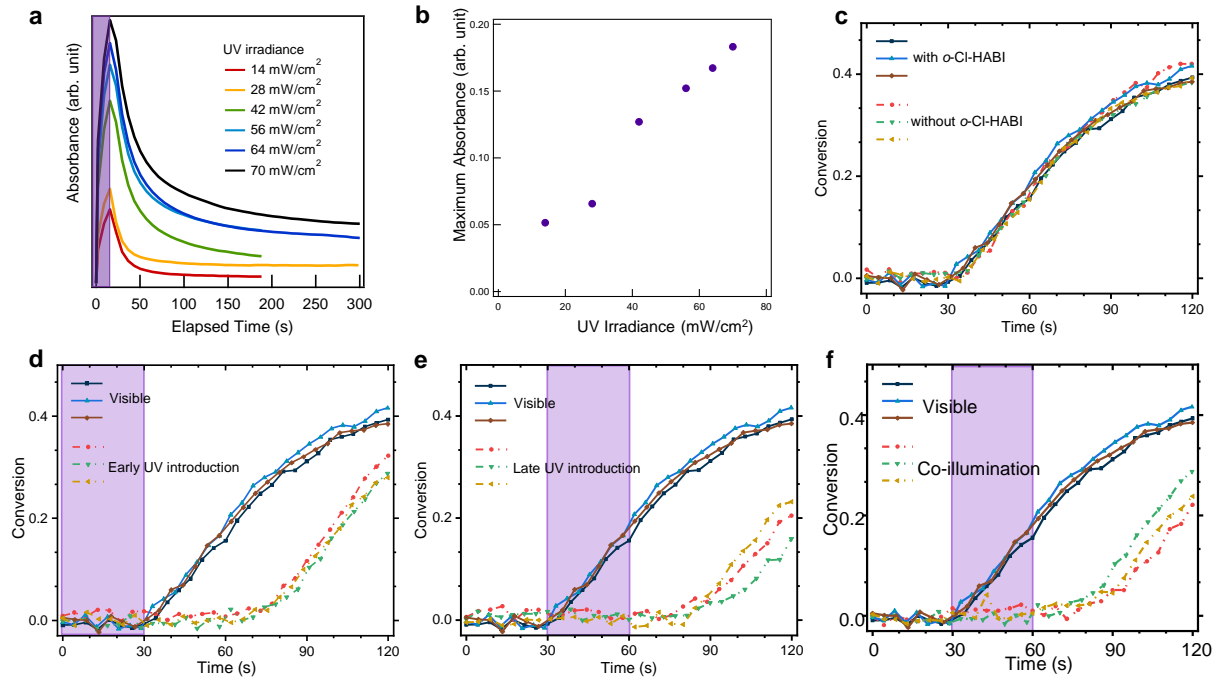


FIGURE CAPTIONS

Fig. 1 Binary photoinhibitory system (BPS) for tomographic vat photopolymerization. a

The concept of binary photoinhibition. In single color printing, all voxels move unidirectionally from $(C_{A0}, 0)$ towards the origin, where polymerization occurs. BPS introduces a stationary state (SS) for each voxel individually. By changing the position and the stability of the SS via external stimuli, each voxel can be steered towards a unique fate, e.g., to polymerize or to remain unpolymerized indefinitely. **b-c** Exemplary phase diagrams for voxels of different fates. A polymerizing voxel (**b**), and a voxel that will remain unpolymerized indefinitely (**c**). Warmer color and arrow length indicate the relative speed of a system moving around the phase diagram. **d-f** Double bond conversion of methacrylate based photoresin upon illumination. The irradiance of visible and UV light were 5 mW/cm² and 30 mW/cm², respectively. “Concurrent” means both sources were on, without *o*-Cl-HABI (**d**) ; UV led to polymerization because of the weak UV absorption induced by CQ (Supplementary Fig. 7). Conversion in M-3 (**e**), UV prolonged the inductive period. Resin M-3 was illuminated continuously by visible light, and intermittently by UV (**f**) (shaded, 30 s each). UV could not revert the polymerization but could effectively arrest the conversion. **g** Illustration of the dual-color tomographic vat photopolymerization assembly of which detailed components presented in Supplementary Figure 1. **h-i** Hollowed tube printed using DCTVP and Resin M-1. Patterns projected from the two light sources (**h**). Rotation period was 24 s and exposure time was 48 for visible light and 54 for UV. Photos of the workpiece (**i**). The inner diameter was defined by the width of the UV stripe while the outer diameter by the visible (blue) stripe. Scale bar: 3 mm.

Fig. 2 Impact of removing negativity constraint (NNC) on printing. **a** Simulated evolution of Jaccard index (J) as a measure of print accuracy with (SC-) and without (DC) NNC. SC-1: negativities are set to zero; SC-2: negativities are eliminated iteratively during sinogram computation; DC: negativities are projected as UV signals. See also Supplementary Figure 16. **b** Zoom-in of the dashed box in A. **c** Simulated over-exposure if process window is missed. **d** Experimentally determined cuboid printing accuracy as a function of printing time. Error bars are standard deviation of triplicates. Shaded areas show process windows for $J = 0.9$. **e** Cross sections of printed cuboids obtained using a 3Shape E4 scanner. **f** Speeding up by shortening induction. Induction is needed in single color mode to build up dose contrast (SC w/o flushing). To increase printing speed, induction can be shortened by removing pre-dissolved radical scavengers (e.g., via white light flushing), which may lead to severe over-exposure (SC w/ flushing). In dual color mode, however, photochemical negativities effectively prevented over-exposure (DC w/ flushing). Scale bars are 5 mm. **g-i** Property modulation through greyscale printing. The left half of the heart shape receives 50% of visible light dose of that by the right half in each rotation. Workpiece at $t = 48$ s in dual color printing (**g**). Workpiece at $t = 46$ s in single color printing (**h**). Compressive modulus of the mechanically differentiated halves (**i**). Similar contrasts were attained, while the achievable softness was improved from 1.43 MPa to 0.68 MPa by introducing negativity. Error bars are standard deviation of triplicates (DC) or duplicates (SC). Scale bars are 3 mm.

Fig. 3 Deviation from the ideal binary photoinhibitory system. a-b Generation of lophyl radicals via UV stimulus. Absorbance was measured at 557 nm at an interval of 6.9 s at various stimulating strengths. Resin M-1 was first flushed with white light for 15 s to remove pre-dissolved oxygen, then illuminated by UV at varied irradiance for 20 s. The decay of absorbance indicated that the self-recombination of lophyl radicals was slow enough to be comparable with and cumulative in a printing process (a). The maximum absorbance scaled linearly with UV irradiance, indicating good lophyl generation capacity (b). **c-f** Sensitivity of conversion to the timing of UV illumination. The irradiance of visible and UV light were 3 mW/cm² and 30 mW/cm², respectively. No UV illumination (c). Solid lines: Resin M-3; dashed lines: without *o*-Cl-HABI. The induction was ~30 s. Early UV introduction (d) (M-3). Solid lines: no UV. Dashed lines: resin illuminated by UV for 30 s (shaded) before introducing visible light. Induction period was ~38 s. Late UV introduction (e) (M-3). Solid line: no UV. Dashed lines: resin illuminated by visible light source alone for 30 s, then by UV alone for another 30 s (shaded), then by visible light again until crosslinking. Induction was ~50 s. All tests were repeated 3 times. Co-illumination (f) (M-3). Solid lines: no UV. Dashed lines: continuously illumination from visible light source with 30 s of UV co-illumination (shaded). Induction period was ~68 s.

REFERENCES

1. Kelly BE, Bhattacharya I, Heidari H, Shusteff M, Spadaccini CM, Taylor HK. Volumetric additive manufacturing via tomographic reconstruction. *Science* **363**, 1075-1079 (2019).
2. Loterie D, Delrot P, Moser C. High-resolution tomographic volumetric additive manufacturing. *Nat Commun* **11**, 852 (2020).
3. Wang B, *et al.* Stiffness control in dual color tomographic volumetric 3D printing. *Nat Commun* **13**, 367 (2022).
4. Bernal PN, *et al.* Volumetric Bioprinting of Complex Living-Tissue Constructs within Seconds. *Adv Mater* **31**, e1904209 (2019).
5. Cook CC, *et al.* Highly Tunable Thiol-Ene Photoresins for Volumetric Additive Manufacturing. *Adv Mater* **32**, e2003376 (2020).
6. Kollep M, *et al.* Tomographic Volumetric Additive Manufacturing of Silicon Oxycarbide Ceramics. *Advanced Engineering Materials*, 2101345 (2022).
7. Toombs JT, *et al.* Volumetric additive manufacturing of silica glass with microscale computed axial lithography. *Science* **376**, 308-312 (2022).
8. Bhattacharya I, Toombs J, Taylor H. High fidelity volumetric additive manufacturing. *Addit Manuf* **47**, 102299 (2021).
9. Rackson CM, *et al.* Object-Space Optimization of Tomographic Reconstructions for Additive Manufacturing. *Addit Manuf* **48**, 102367 (2021).
10. van der Laan HL, Burns MA, Scott TF. Volumetric Photopolymerization Confinement through Dual-Wavelength Photoinitiation and Photoinhibition. *ACS Macro Letters* **8**, 899-904 (2019).
11. de Beer MP, van der Laan HL, Cole MA, Whelan RJ, Burns MA, Scott TF. Rapid, continuous additive manufacturing by volumetric polymerization inhibition patterning. *Sci Adv* **5**, eaau8723 (2019).
12. Feldkamp LA, Davis LC, Kress JW. Practical cone-beam algorithm. *Journal of the Optical Society of America A* **1**, 612-619 (1984).

13. Garland M, Heckbert PS. Surface simplification using quadric error metrics. In: *Proceedings of the 24th annual conference on Computer graphics and interactive techniques* (1997).
14. Bærentzen A, Rotenberg E. Skeletonization via local separators. *ACM Transactions on Graphics (TOG)* **40**, 1-18 (2021).
15. Zhang C, Chen T. Efficient feature extraction for 2D/3D objects in mesh representation. In: *Proceedings 2001 International Conference on Image Processing (Cat. No. 01CH37205)*. IEEE (2001).
16. Jacobson A, Kavan L, Sorkine-Hornung O. Robust inside-outside segmentation using generalized winding numbers. *ACM Trans Graph* **32**, Article 33 (2013).
17. Bærentzen JA, Gravesen J, Anton F, Aanæs H. 3D Surface Registration via Iterative Closest Point (ICP). In: *Guide to Computational Geometry Processing: Foundations, Algorithms, and Methods* (eds Bærentzen JA, Gravesen J, Anton F, Aanæs H). Springer London (2012).

Data availability

All data analyzed in this manuscript are included in the main text or the extended data.

Code availability

MATLAB code used to visualize data is available upon request.

Acknowledgements

We thank Mark Smith and 3Shape A/S for providing the top model of 3Shape E-series laboratory scanners. We thank Josefine F. Lønholdt, Jane Pedersen, Prof. Yan Wei, Dr. Stefan Bruns and Christina Schmidleithner for helpful discussions and resource acquisition, Dr. Mariusz Kubus for assistance in FTIR measurement, Peter R. Stubbe for guidance in mechanical testing, Ishaq Khaliqdad and Andreas G. Pedersen for TVP prototyping, Christina B. Nielsen for assistance in chemical analysis and management. We are grateful to the 3D Imaging Center at the Technical University of Denmark for providing access to X-ray tomography equipment and the Thingiverse community for creating high quality STL files for 3D printing research. YY gratefully acknowledges financial support from the Villum Foundation (Grant No. 40805), the Independent Research Fund Denmark (Grants No. 0136-00043 and 8022-00162) and DTU Skylab (2 DGs and a PoC). BW and AI are grateful for the support from the China Scholarship Council (Grant No. 202006130009).

Author contributions

Y.Y. conceptualized the research. B.W. and Y.Y. designed the methodologies. B.W. led and, with W.S., J.P.C.N., H.S.M., T.D.V.C. and A.A.S., carried out the experimental investigations. J.R.F. and Y.Y. contributed to the modelling of light-matter interactions and reactive transport. K.A., A.I. and Y.Y. acquired the resources needed to carry out the research. Y.Y. administered

the collaboration. J.R.F, H.O.S., K.A., A.I. and Y.Y co-supervised the research. B.W. and Y.Y. wrote the original draft. All authors reviewed and edited the submitted manuscript.

Competing interests

YY declares that a patent has been filed related to the topic covered in this publication. The remaining authors declare no competing interests.

Additional information

Supplementary information

Supplementary information is provided in a separate file which contains Supplementary Note, Supplementary Equations, Supplementary Figures and Supplementary Tables. 8 Supplementary Videos are also available.

Correspondence and requests for materials

Correspondence to Yi Yang (yyan@dtu.dk)

Supplementary Information for

Creating negative illumination for tomographic 3D Printing via binary photoinhibition

Bin Wang, Weichao Sun, Jadze P. C. Narag, Hossein S. Mozajin, Thor D. V. Christiansen, Jeppe R. Frisvad, Adrian A. Schiefler, Henning O. Sørensen, Kristoffer Almdal, Aminul Islam, Yi Yang

Correspondence to: Yi Yang, (email: yyan@dtu.dk)

This PDF file includes:

Supplementary Note
Supplementary Equations 1-8
Supplementary Figures 1-23
Supplementary Tables 1-2
Captions for Supplementary Movies 1-8
References

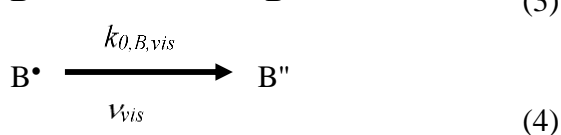
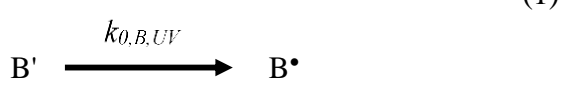
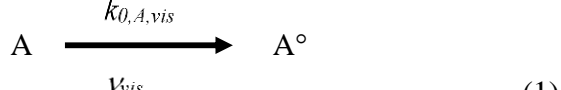
Other Supplementary Materials for this manuscript include the following:

Supplementary Movies 1-8

Supplementary Note

Behavior of an ideal binary photoinhibitory system

The scheme of an ideal binary photoinhibitory system (BPS) given by Eqs 1-2 can be represented as



A and B' are present in the reaction at the outset. A and B[•] are polymerization inhibitors whereas the rest of the species are inert in the photopolymerization context. However, A[°] and B'' are excited state and must therefore be expected to engage in reaction or thermally relax back to A and B[•]. Note that step Supplementary Eq. 3 is a simplification¹⁸ and yields a constant half-life. The scheme offers a means to navigate the phase diagram for each voxel individually by adjusting the strength of irradiation using two coordinated light sources (P_{UV} and P_{vis}). Figs 1b-c show the diagrams for a voxel that will (b) and one that will not (c) polymerize. Given an illumination profile ($P_{UV}(t)$ and $P_{vis}(t)$), the steering trajectory of a BPS depends on three parameters

$$\alpha = k_{0,B,vis} / k_{0,A,vis}, \quad (5)$$

$$\beta = \frac{k_{0,B,UV} P_{UV}}{k_{0,A,vis} P_{vis}}, \text{ and} \quad (6)$$

$$\lambda = \ln 2 / k_{1,B}. \quad (7)$$

Supplementary Fig. 18 compiles the influences of these parameters. The parameter α marks the relative sensitivity of the two inhibitory species to visible light, whereas β represents the strength of UV as the “negative” illumination. Greater α indicates greater energy requirement in order to create an unpolymerized stationary state (SS). The difference between a polymerizing SS and an unpolymerized SS is more pronounced with greater β (UV irradiance) as well as a longer half-life for B (λ). In practice, the irradiation received by a voxel varies periodically due to the rotation of the curing volume, and the system status is steered temporally. Supplementary Movie 1 shows an example of how phase diagram evolves at a constant projector output when a voxel in question is not located at the rotation axis. We define the efficiency of UV as “negative” illumination using

$$W = \int_{\varepsilon}^1 \frac{C_B}{C_A} d \left(\frac{C_A}{C_{A0}} \right), \quad (8)$$

where the lower limit of the integral ε is the normalized concentration of Species A that would initiate polymerization in the absence of B. When $W = 1$, a BPS doubles the induction

period before a voxel polymerizes, and the UV matches the visible light by delivering negative illumination with the same intensity unit, i.e., a sinogram containing both signs can be divided into a positive part for S1 and a negative part for S2 without additional adjustment of grayscale intensity. Light extinction in the curing volume, however, creates spatial variance of W . Supplementary Fig. 19 shows the impact of extinction coefficient (μ) on achievable W at five different radial positions, when absorption is not the main cause for light attenuation. The scattered data were obtained by tracking voxels at a fixed radial position but a randomized starting angle. The closer a voxel is to the edge of the curing volume, the more sensitive its W will be to the rotation periodicity. At constant UV output, negativity efficiency reduces towards the rotation center. This spatial loss of efficiency cannot be compensated by simply increasing the output power because the diffusion of excessive radical scavengers generated at large radial distances will cause undesired underexposure. As a result, formulating a BPS can be demanding in that it requires good balance between transparency and absorptivity in at least two wavelength regimes.

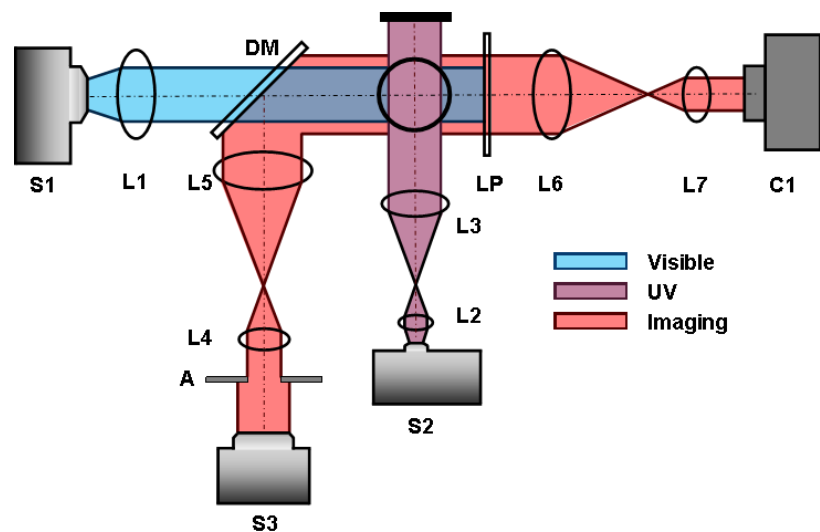
In contrast to photoinhibitors used in more conventional light-based additive manufacturing methods, a stable Species B with a long lifespan is favored in a BPS designed for tomographic printing because of the cumulative nature of the latter. Supplementary Fig. 20 shows the impact of half-life on achievable W at three radial positions at constant UV irradiation. The energy that powers the UV irradiation is spent to counteract the overspent doses of visible light that would lead to over-exposure. As a result, a dual color printer uses more energy than its single-color counterpart for printing the same geometry. The UV doses needed to reach $W = 1$ in Supplementary Fig. 21 shows the sensitivity of the minimum energy requirement for producing equivalent negative illumination across the curing volume for three extinction factors.

Deviation from the ideal binary photoinhibitory system

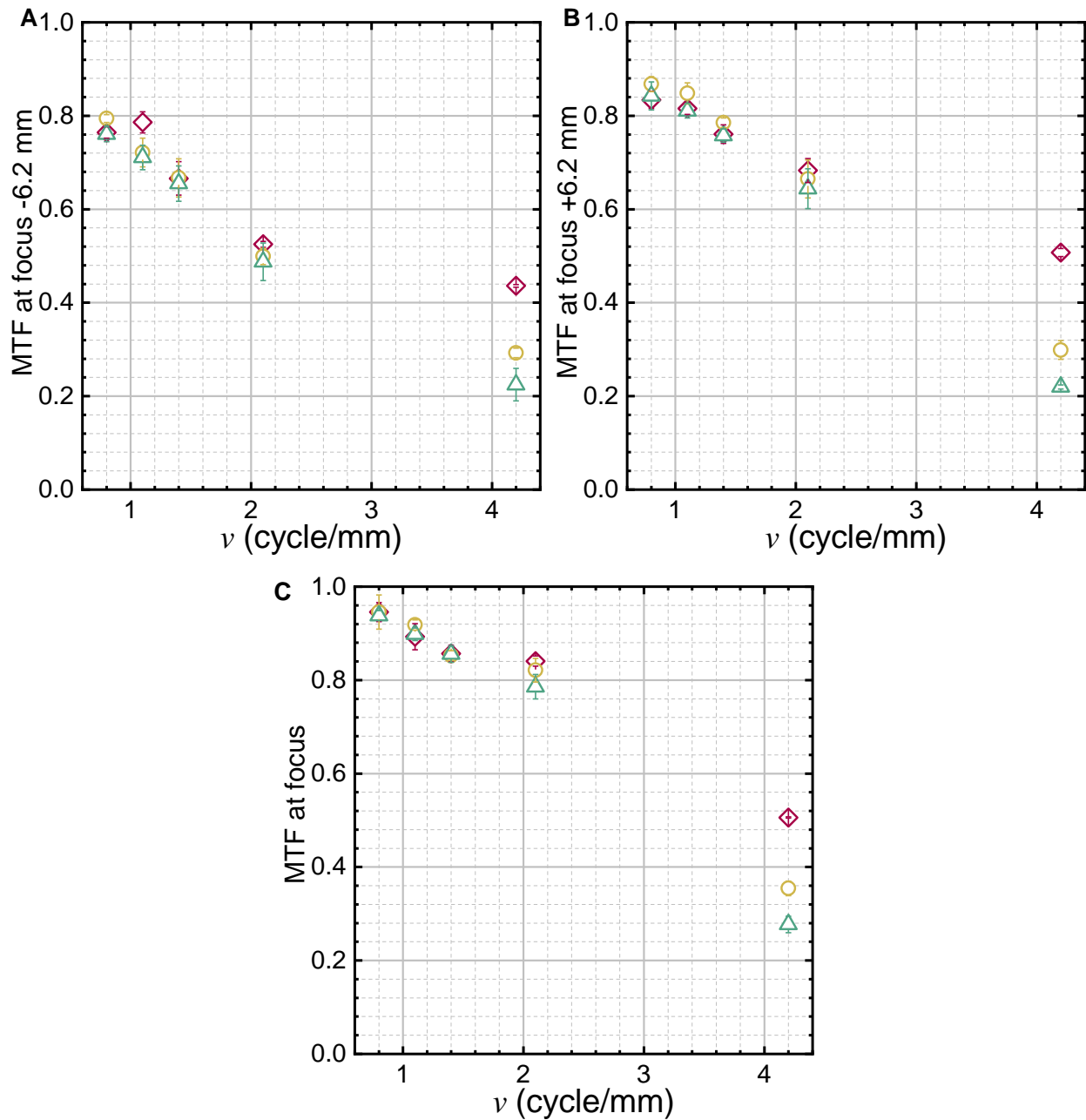
The oxygen-lophyl system we employed to demonstrate the advantages of a BPS differs from the ideal BPS system in that the lophyl-generation capacity of the photoresin under external stimulus is limited. A prerequisite for indefinitely pinning the binary system at an SS other than the origin is an unlimited supply of Species B upon UV illumination. An abundant supply does not guarantee more efficient negativity generation, as the lifespan of Species B often becomes the bottleneck, but a shortage of supply prevents a BPS from properly functioning (Supplementary Fig. 22). In this study, the lophyl radical that served as Species B was generated from photolysis of *o*-Cl-HABI. We found that 1 wt% *o*-Cl-HABI (recipe M-1) sufficed to generate lophyl radicals that clearly demonstrated the advantages of a BPS. Higher concentrations led to stronger light extinction (Supplementary Fig. 23) that would deteriorate workpiece fidelity towards the rotation center.

Supplementary Movie 3 shows a simulated dual color printing process in which the limited *o*-Cl-HABI and its effect on light extinction coefficients are accounted for. Supplementary Movie 2 shows the evolution of the BPS for two voxels of interests (A – unpolymerized, B – polymerized) and Supplementary Movie 4 shows the same geometry printed using single color mode.

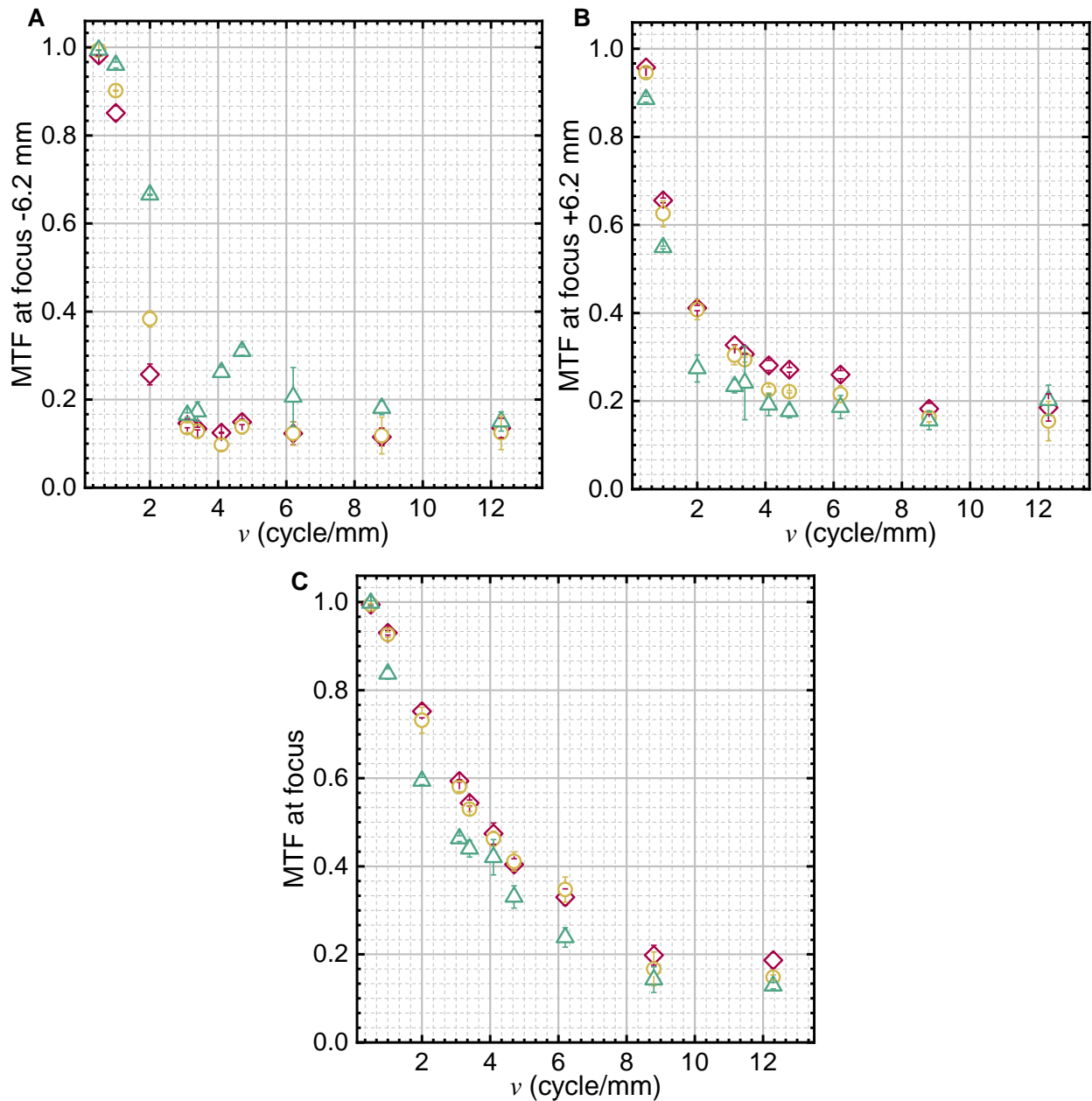
Supplementary Figures 1-23



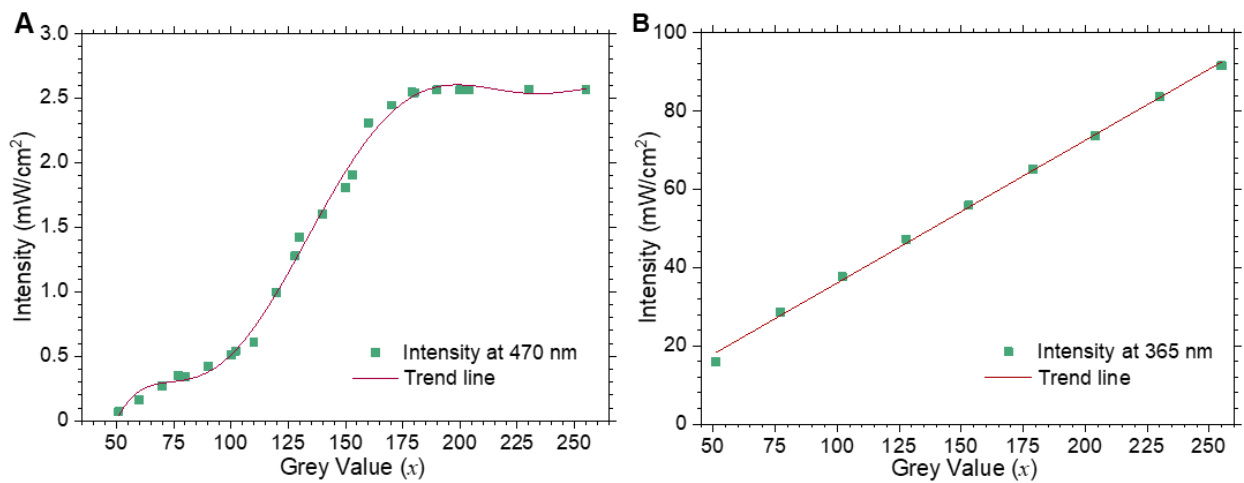
Supplementary Figure 1. Schematic illustration of the dual-color tomographic vat photopolymerization assembly. All optomechanical parts are tabulated in Supplementary Table 1.



Supplementary Figure 2. Modulation transfer function of visible light projection. Red diamond, yellow circle, and green triangle are the results at (0, 0) (3.1, 5.5) (6.2, 11), respectively. **(A)** MTF at focus -6.2 mm, i.e., the plane 6.2 mm closer to S1 than the focal plane. **(B)** MTF at focus +6.2 mm, i.e., the plane 6.2 mm farther away from the focal plane. **(C)** MTF at the focal plane.

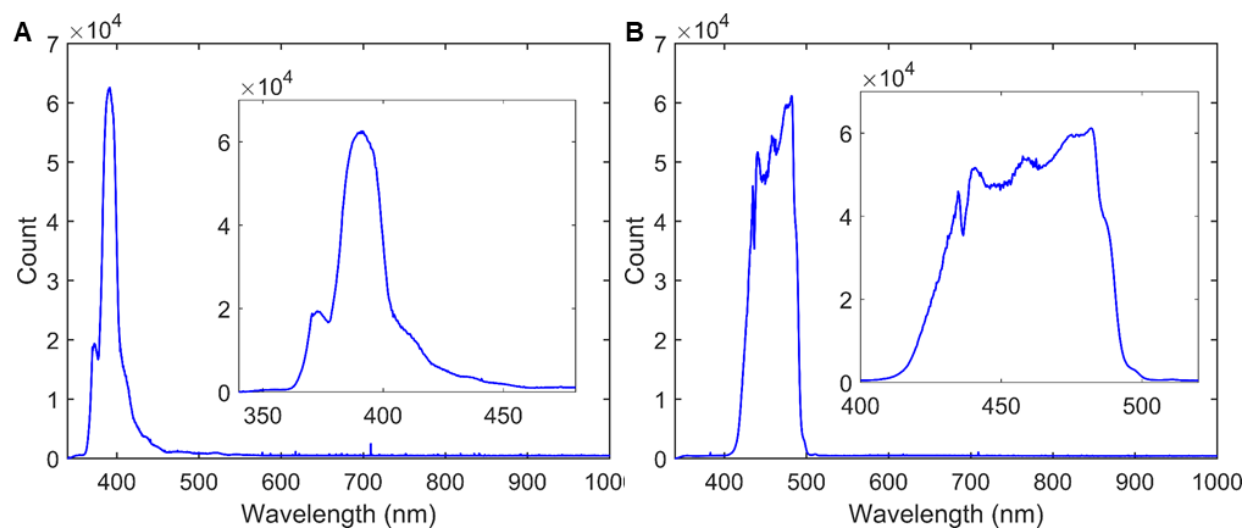


Supplementary Figure 3. Modulation transfer function of UV projection. Red diamond, yellow circle, and green triangle are the results at (0, 0) (3.1, 5.5) (6.2, 11), respectively. **(A)** MTF at focus -6.2 mm, i.e., the plane 6.2 mm closer to S2 than the focal plane. **(B)** MTF at focus +6.2 mm, i.e., the plane 6.2 mm farther away from the focal plane. **(C)** MTF at the focal plane.

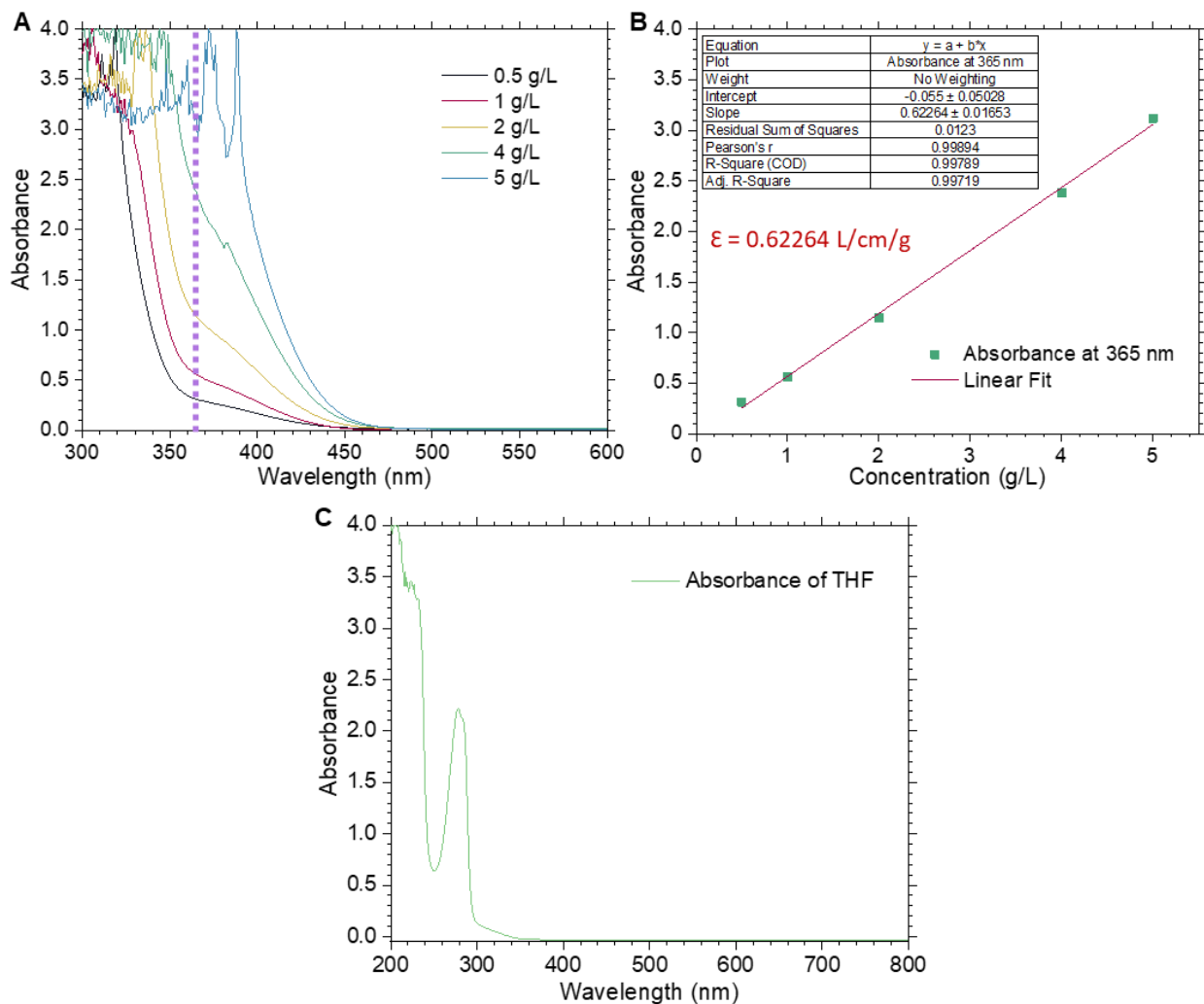


Supplementary Figure 4. Irradiation intensity as a function of pixel grey value.

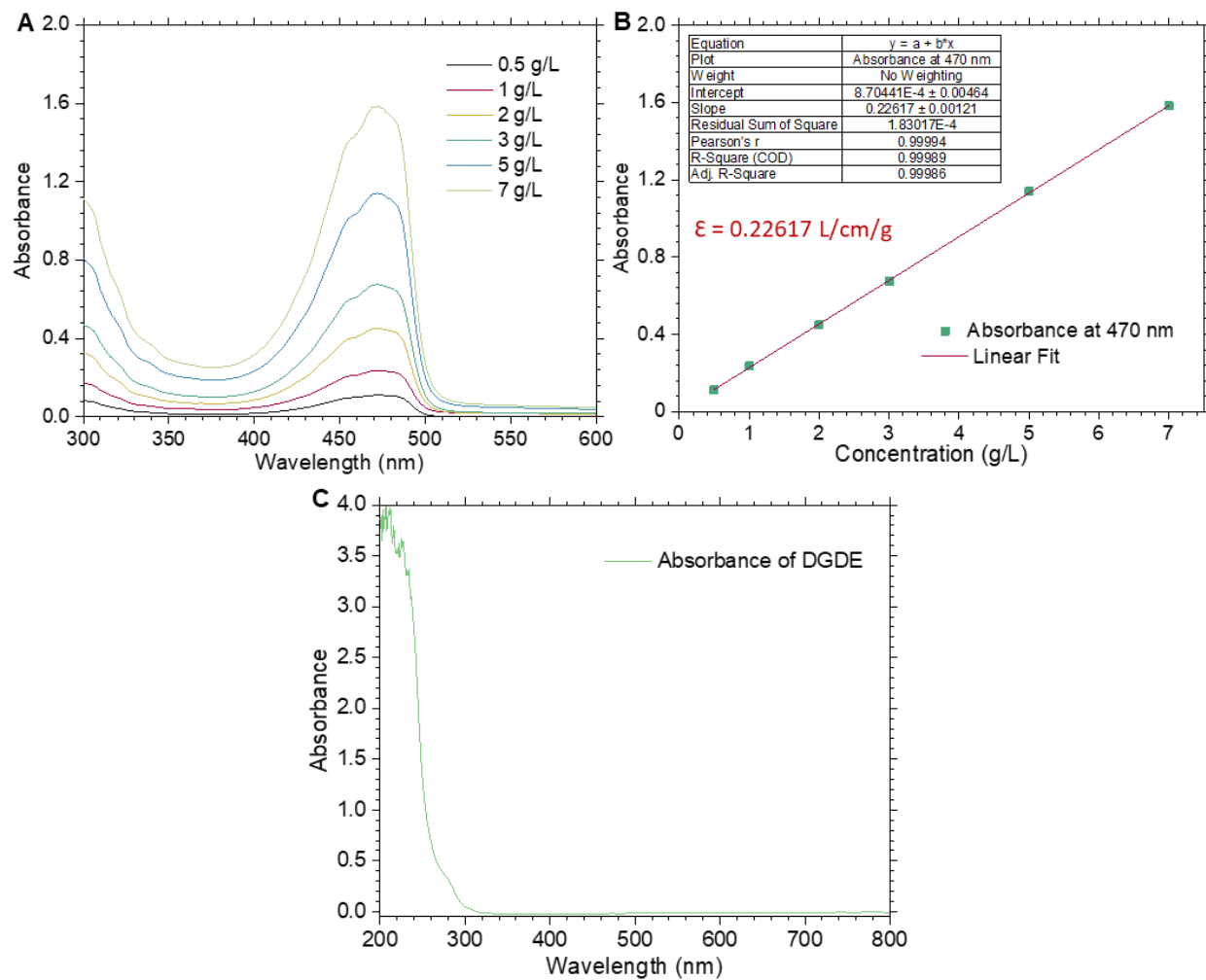
Irradiance was measured at the focal plane using a photodiode power sensor. Trend lines are added for visual aid. (A) Irradiation from S1 at 470 nm. (B) Irradiation from S2 at 365 nm.



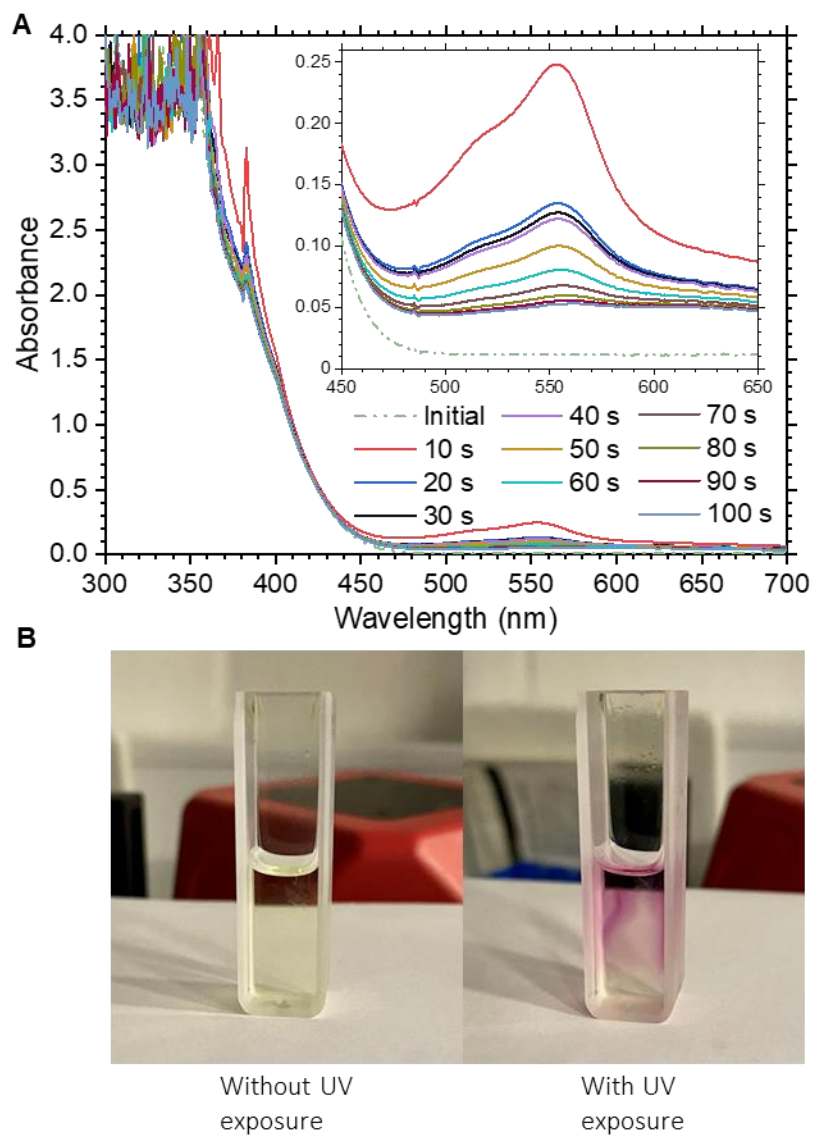
Supplementary Figure 5. Output spectra of the light sources. Measured by a spectrometer placed at the focal plane. **(A)** UV, with maximum output between 365 nm and 385 nm. **(B)** White flushing from the visible light source, with wavelength greater than 490 nm being cut off by the dichroic mirror.



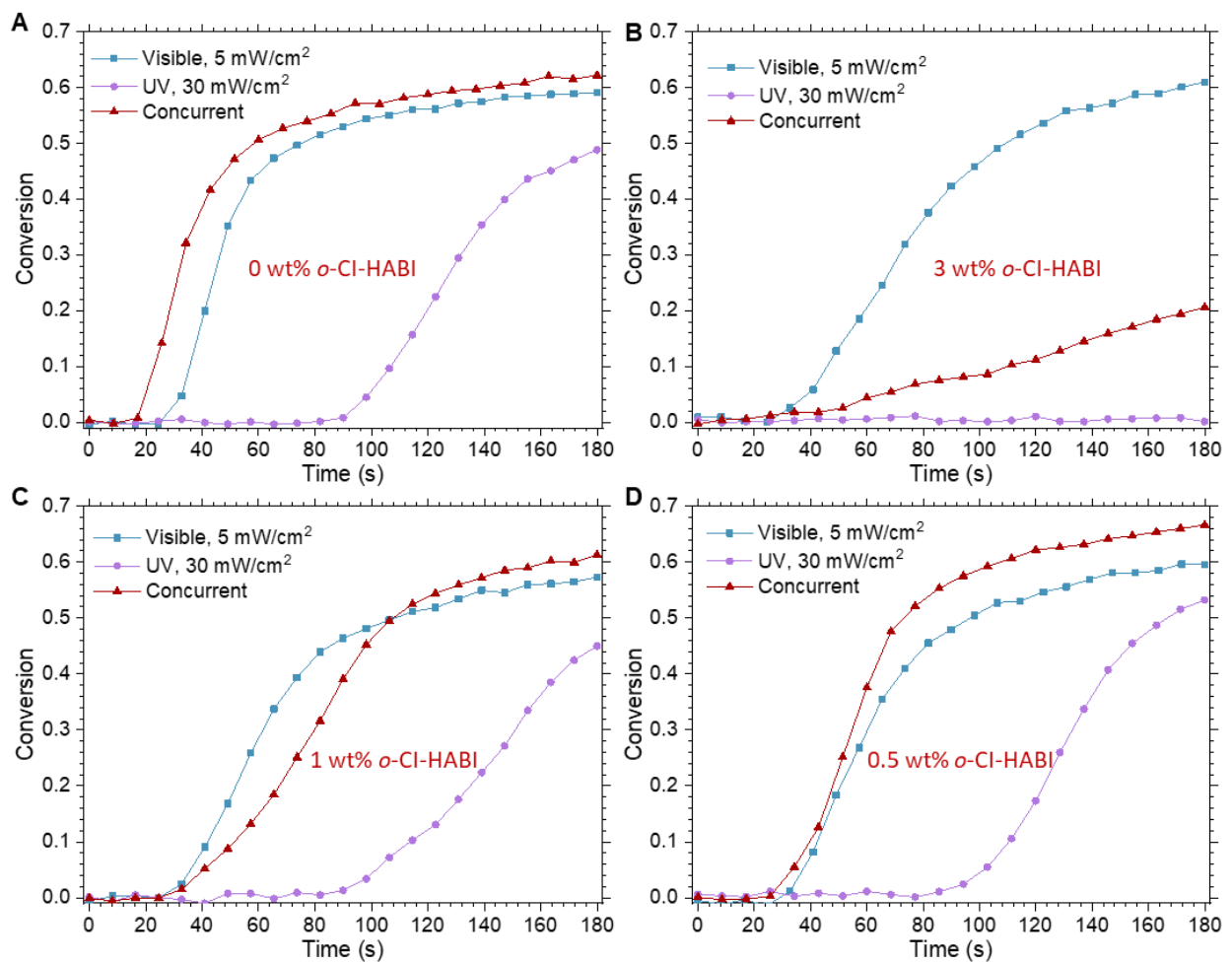
Supplementary Figure 6. UV-Vis spectroscopy for *o*-Cl-HABI and THF. (A) Absorption profiles at various *o*-Cl-HABI concentrations. (B) Fitted absorption data for calculating extinction coefficient at 365 nm. (C) Absorption profile of the solvent THF. There is no absorption of THF near 365 nm or in the visible range, indicating that the effect of THF on the optical properties of the photoresin associated with tomographic printing is limited.



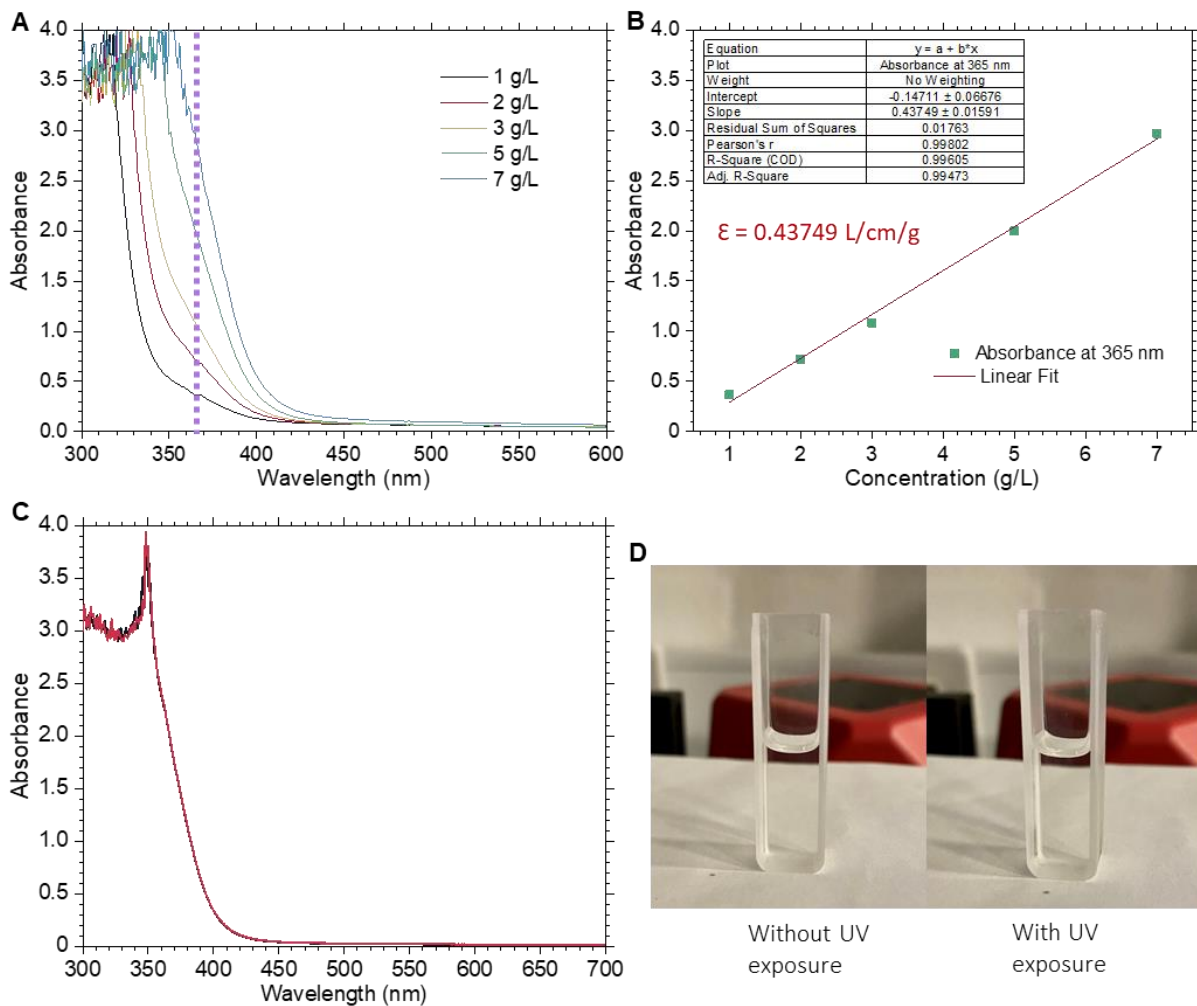
Supplementary Figure 7. UV-Vis spectroscopy for CQ. (A) Absorption profiles at various CQ concentrations. (B) Calculation of extinction coefficient of CQ at 470 nm. (C) Absorption profile of the solvent DGDE, no absorption in the visible wavelength regime was identified.



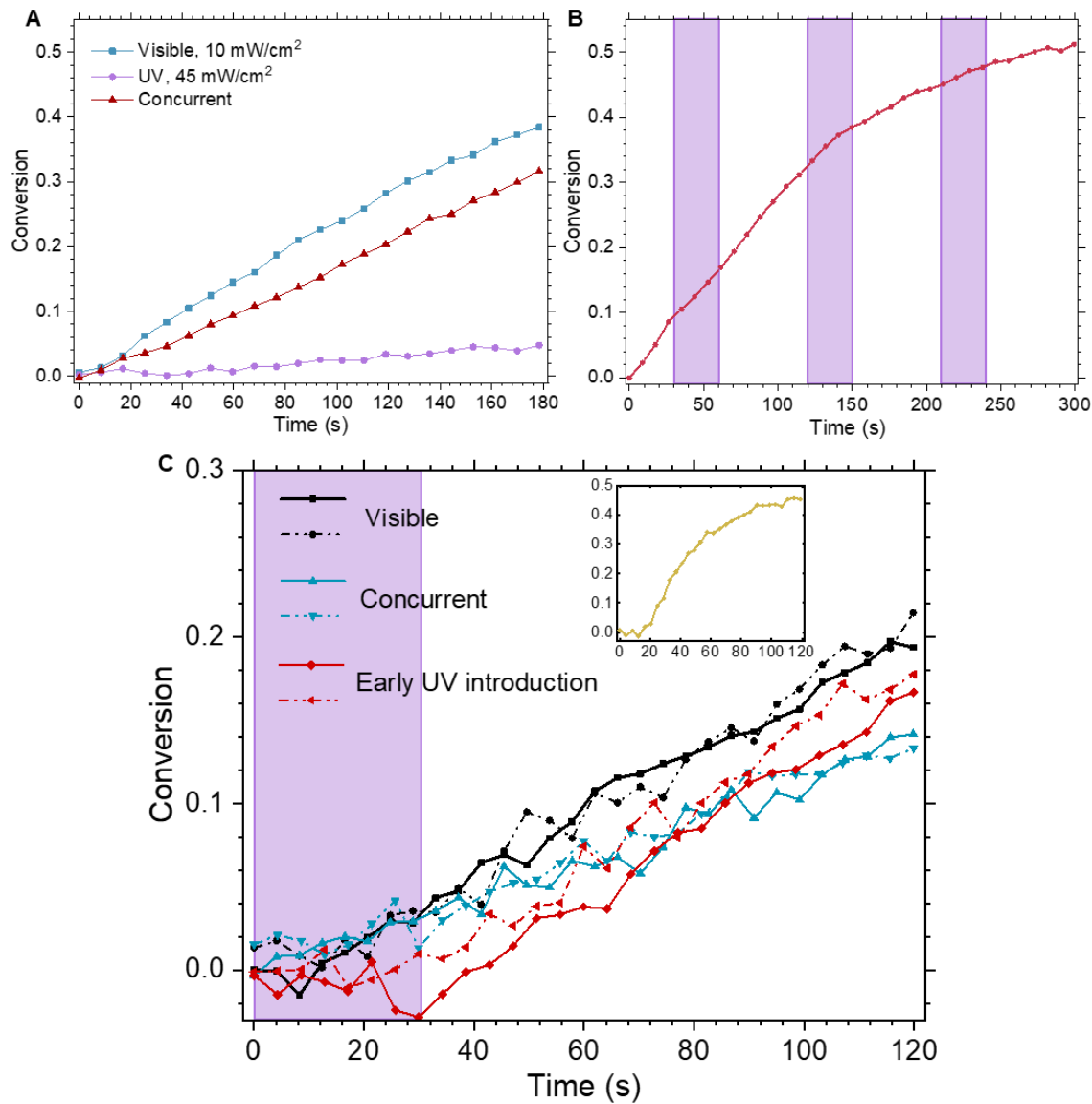
Supplementary Figure 8. UV-Vis measurement of the *o*-Cl-HABI solution after UV illumination. (A) After the initial measurement, the sample was illuminated by UV for 30 s at 30 mW/cm², after which an absorbance spectrum was taken every 10 s. The peak near ~555 nm correlates with the transient lophyl concentration and is zoomed-in in the inset. (B) Color change upon *o*-Cl-HABI photolysis corresponding to the peak near 550 nm.



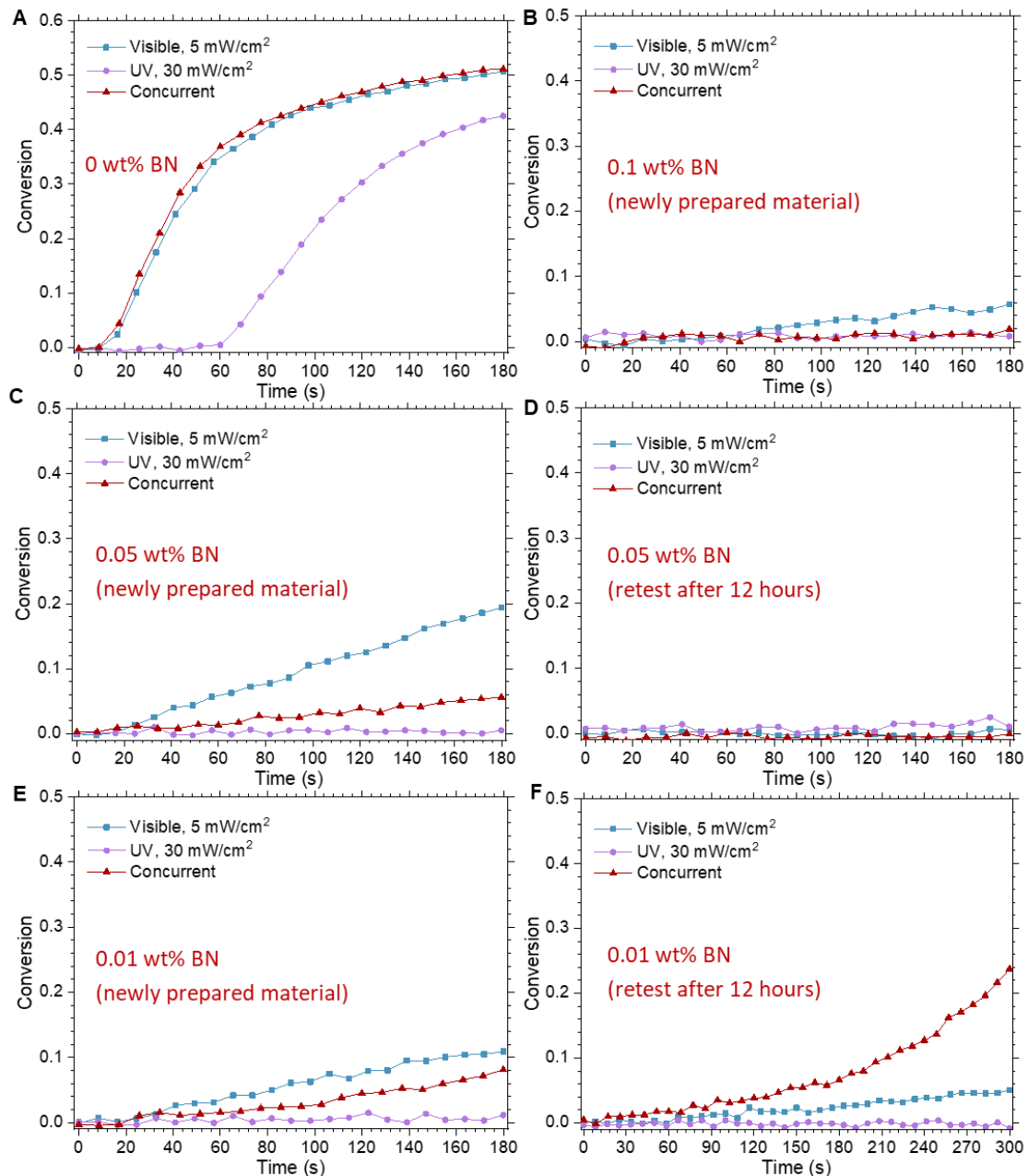
Supplementary Figure 9. Sensitivity of double bond conversion to illumination for diacrylate-based resin at various *o*-Cl-HABI concentrations. The irradiance of visible and UV light were 5 mW/cm² and 30 mW/cm², respectively. “Concurrent” means both sources were on. (A) without *o*-Cl-HABI. (B) 3 wt% *o*-Cl-HABI. (C) 1 wt% *o*-Cl-HABI. (D) 0.5 wt% *o*-Cl-HABI. Higher concentration of *o*-Cl-HABI was needed to delay gelation or inhibit conversion of the BPAGDA/PEGDA resin.



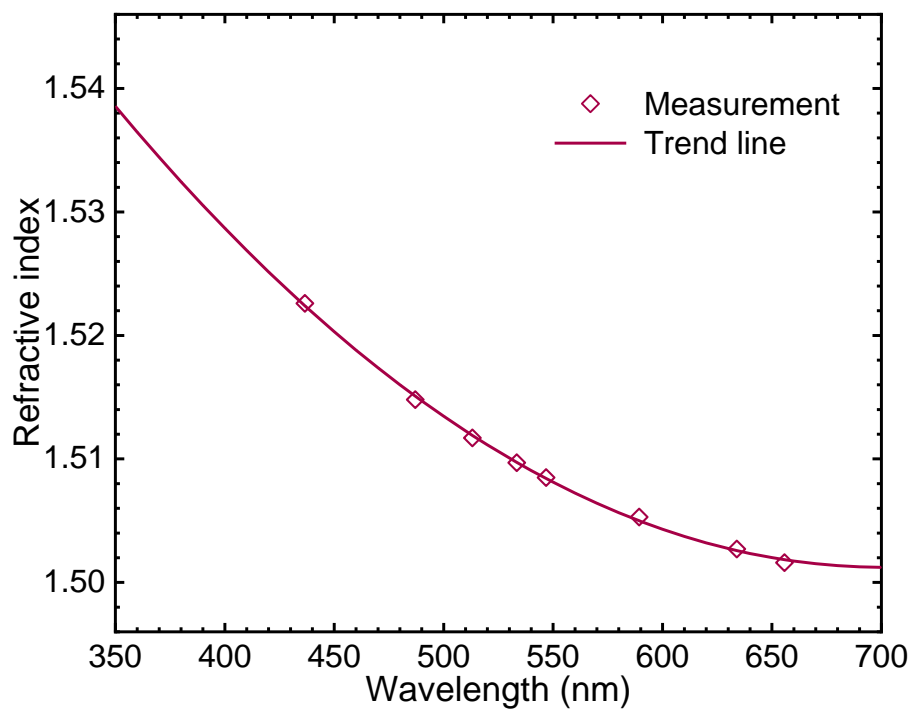
Supplementary Figure 10. UV-Vis spectroscopy for tetraethylthiuram disulfide (TED, CAS#97-77-8, Sigma-Aldrich) in THF. (A) Absorption profiles at various TED concentrations. **(B)** Calculation of extinction coefficient of TED at 365 nm. **(C)** Measurement of the absorption data of the 5 g/L TED in THF in the state without (black line) and with (red line) UV exposure, indicating that there is no absorption change upon UV introduction. **(D)** No color change upon TED photolysis.



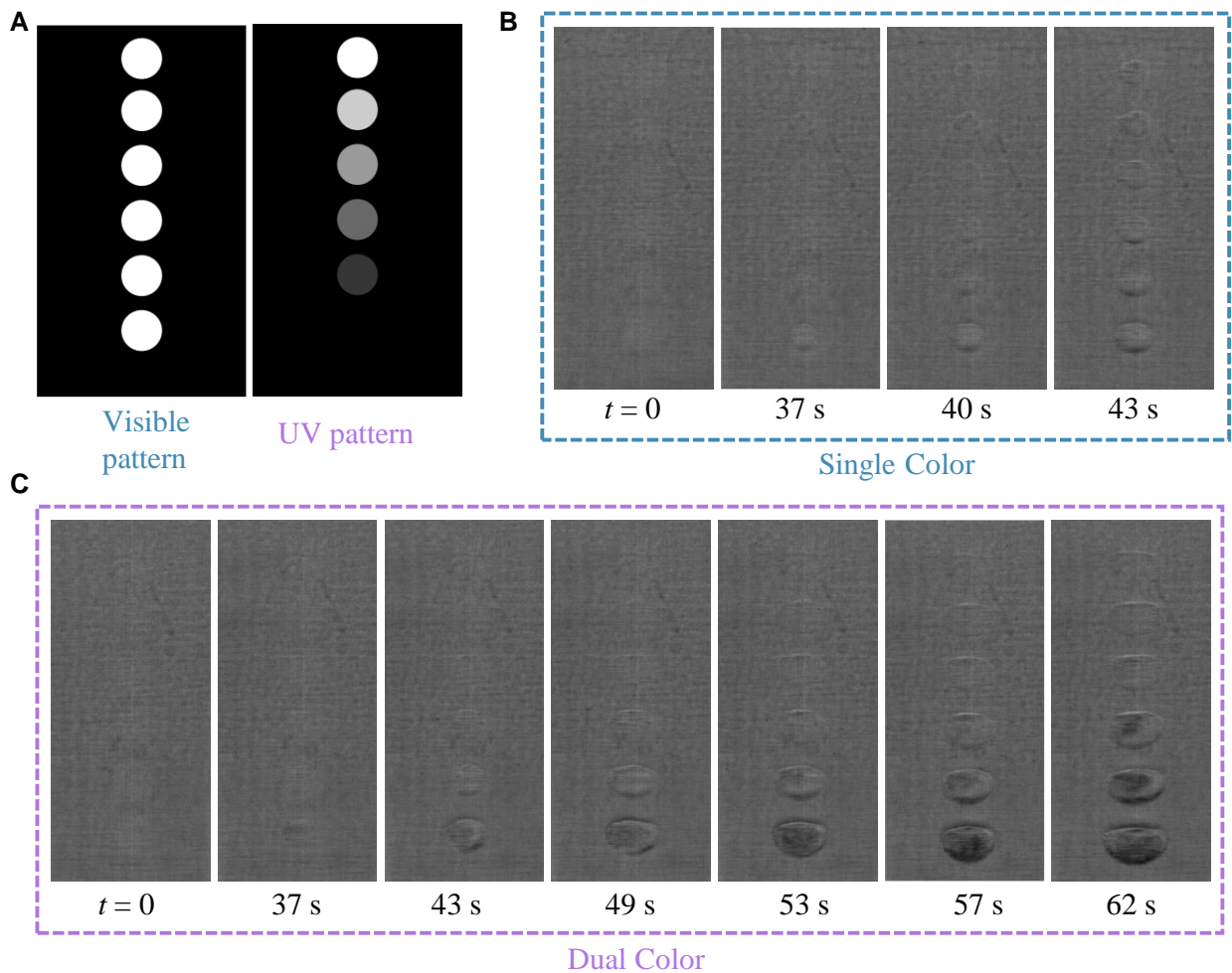
Supplementary Figure 11. Double bond conversion upon illumination for methacrylate-based recipe with 3 wt% TED added as inhibitor. “Concurrent” means both sources were on. (A) Conversion in the resin. The irradiance of visible and UV light were 10 mW/cm² and 45 mW/cm², respectively. (B) Resin was illuminated continuously by visible light (10 mW/cm²), and intermittently by UV (45 mW/cm², shaded, 30 s each). UV weakly arrested the conversion. (C) Sensitivity of conversion to the timing of UV illumination. The irradiance of visible and UV light were 5 mW/cm² and 30 mW/cm², respectively. Black lines: continuous visible light without UV; Blue lines: concurrent visible and UV light; Red lines: early UV introduction for 30 s (shaded) before introducing visible light. UV could not extend the induction period and only mildly inhibited the conversion. Inset shows the conversion of resin without TED under continuously visible light. TED may significantly reduce the polymerization rate of resin.



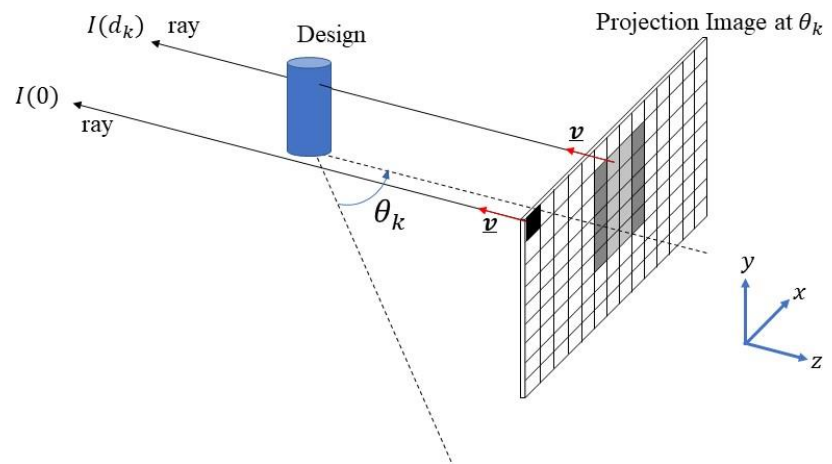
Supplementary Figure 12. Sensitivity of double bond conversion to illumination for methacrylate-based recipe at various of butyl nitrite (BN, CAS# 544-16-1, Sigma-Aldrich) concentrations. BN was used as inhibitor and added to the methacrylate-based formula. The irradiance power of visible and UV light were 5 mW/cm² and 30 mW/cm², respectively. **(A)** without BN. **(B)** 0.1 wt% BN, Measurement was carried out using the newly prepared material **(C)** 0.05 wt% BN. **(D)** 0.05 wt% BN, retested after 12 hours; It shows the different results from that in figure (C). **(E)** 0.01 wt% BN. **(F)** 0.01 wt% BN, retested after 12 hours.



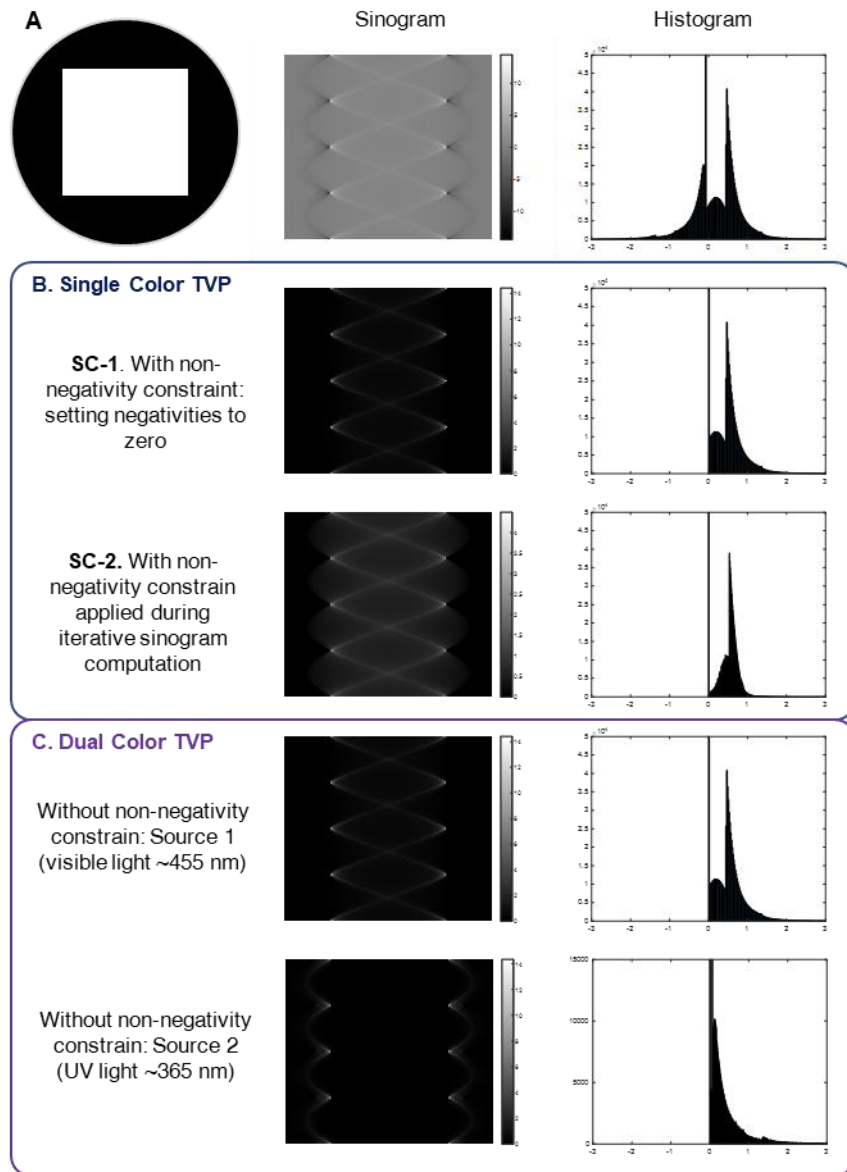
Supplementary Figure 13. Refractive indices of Resin M-1. Refractive indices were measured using an Abbe refractometer (Anton Paar, Austria). Trendlines are added as visual aid.



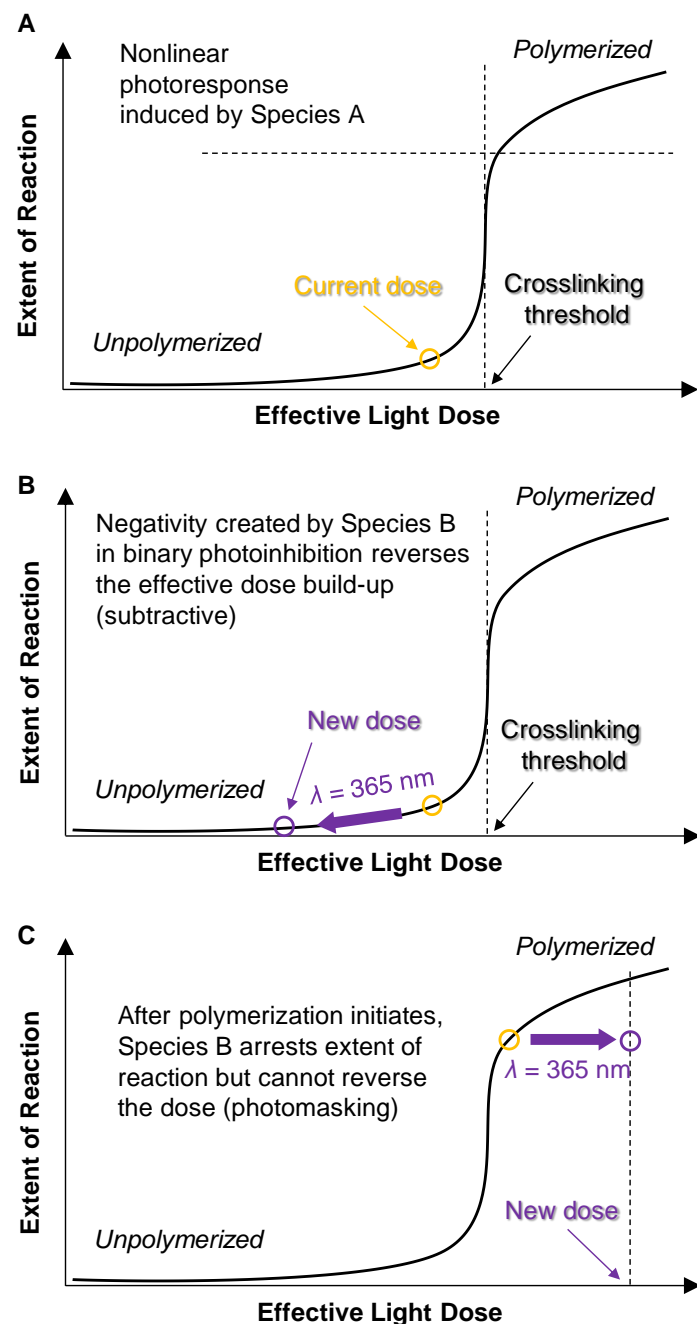
Supplementary Figure 14. Photoresponse of Resin M-1. (A) Projected patterns. S1 (visible) intensity set to 255 for all 6 filled circles. S2 (UV) intensities were (from top to bottom) 255, 205, 155, 105, 55 and 0. (B) Single color printing. Workpieces appeared after 37 s. (C) Dual color printing. All workpieces appeared by 62 s, suggesting $W \leq 0.68$ at the rotation center.



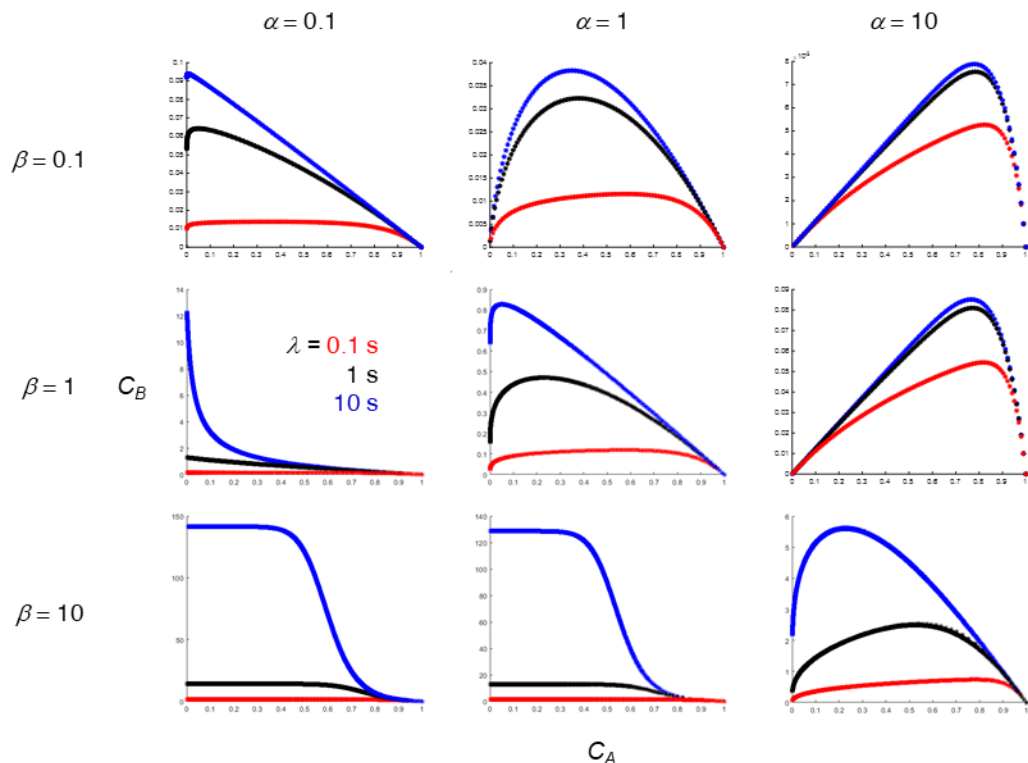
Supplementary Figure 15. Illustration of the sinogram computation using volumetric ray casting.



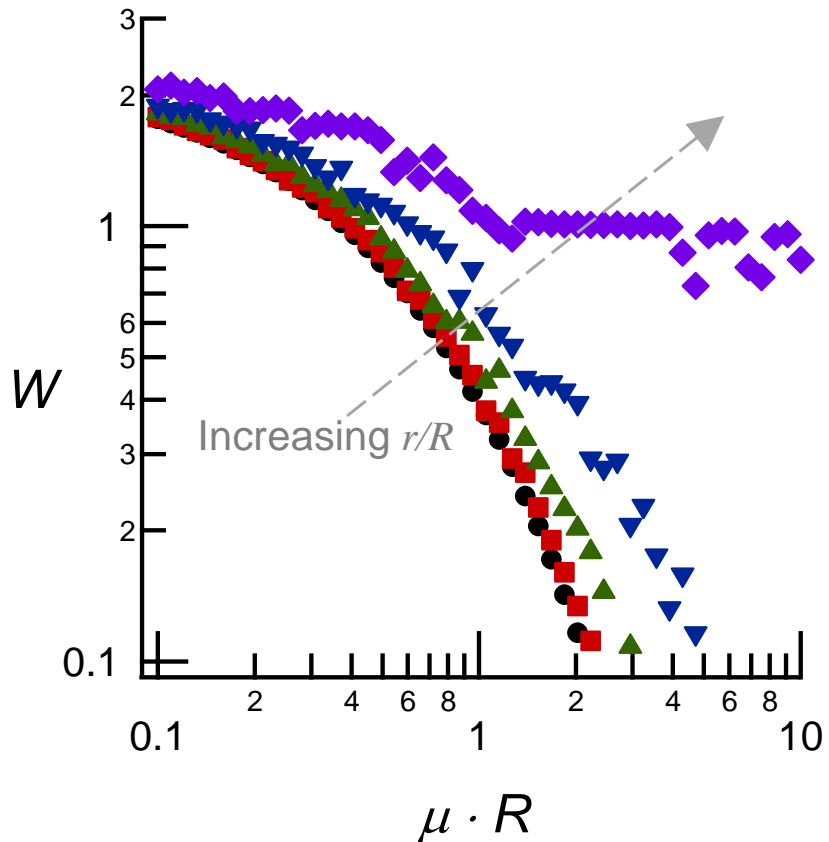
Supplementary Figure 16. Impact of non-negativity constraint. (A) A square and its sinogram computed using the iterative method. The sinogram contains negativities that erase undesired energy build-up. (B) Two methods of handling negativity in single color printing. SC-1: setting all negativities to zero; SC-2: non-negativity constraint applied in each iteration during sinogram computation. SC-2 was employed in our previous study (3). (C) With binary photoinhibition, the positive part of the original sinogram is projected by the visible light source (S1) and the absolute values of the negativities are projected by the UV light source (S2).



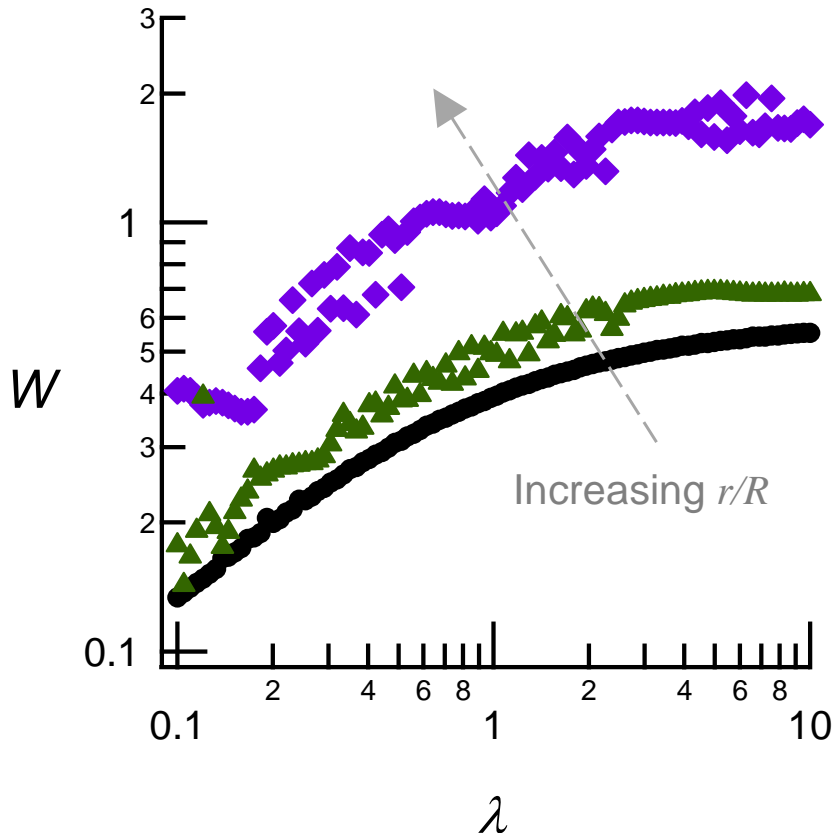
Supplementary Figure 17. Photochemical negativity vs. photomasking. (A) The nonlinear photoresponse required for tomographic printing can be introduced using a single photo inhibitor. (B) Photochemical negativity created via binary photoinhibition reverses the system state along the nonlinear curve, amounting to reducing effective dose build-up, i.e., the effect is subtractive. (C) After polymerization initiates, Species B can only arrest the extent of reaction but not reversing it (photomasking).



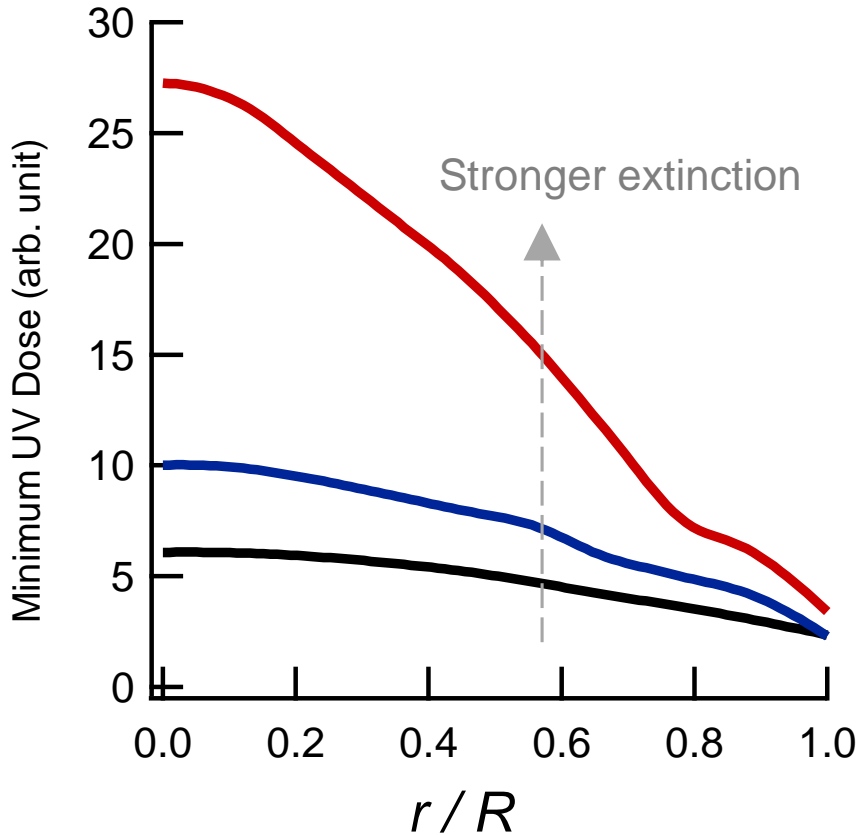
Supplementary Figure 18. Sensitivity of system trajectory to kinetic parameters. α represents the relative sensitivity of the two radical scavengers to visible light illumination. β represents the relative strength of irradiation from the two sources. λ is the half-life of Species B if its decay follows first order kinetic.



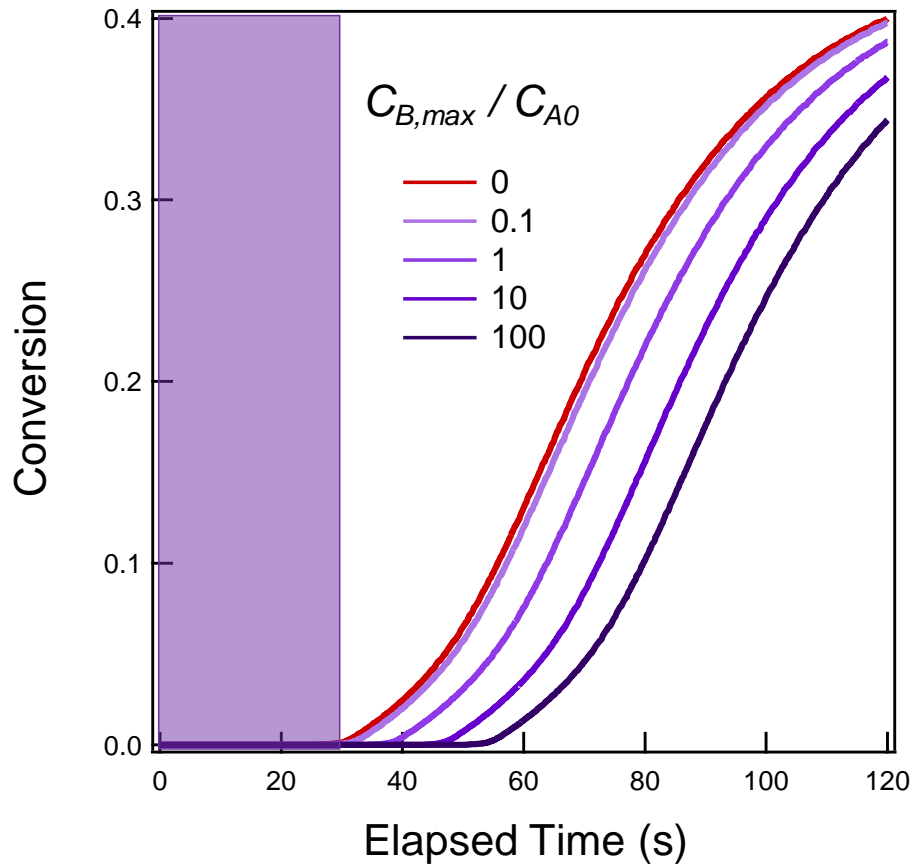
Supplementary Figure 19. Dependence of negativity equivalence (W) on extinction coefficient (μ) at various radial position. Results were obtained from numerical simulations. Each data point corresponds to a simulation of a voxel with a fixed radial position but randomized starting angle. $r/R = 0$ (black), 0.25 (red), 0.50 (green), 0.75 (blue) and 1.0 (purple).



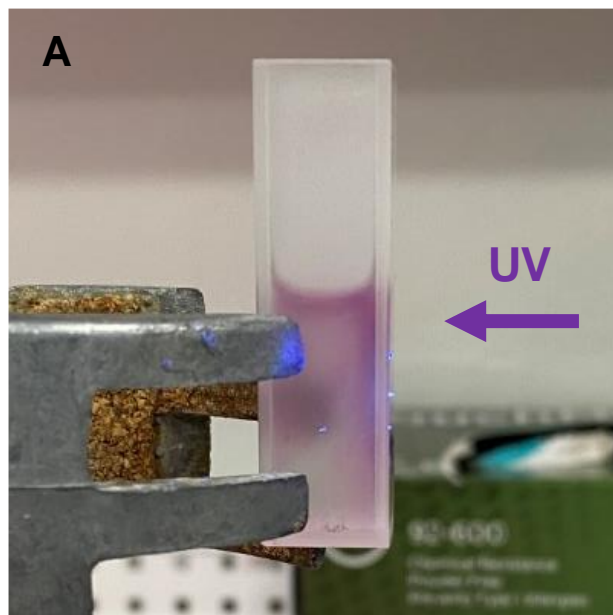
Supplementary Figure 20. Sensitivity of negativity equivalence to the half-life of Species B (λ). Results were obtained from numerical simulations. Each data point corresponds to a simulation of a voxel with a fixed radial position but randomized starting angle. $r/R = 0$ (black), 0.50 (green) and 1.0 (purple).



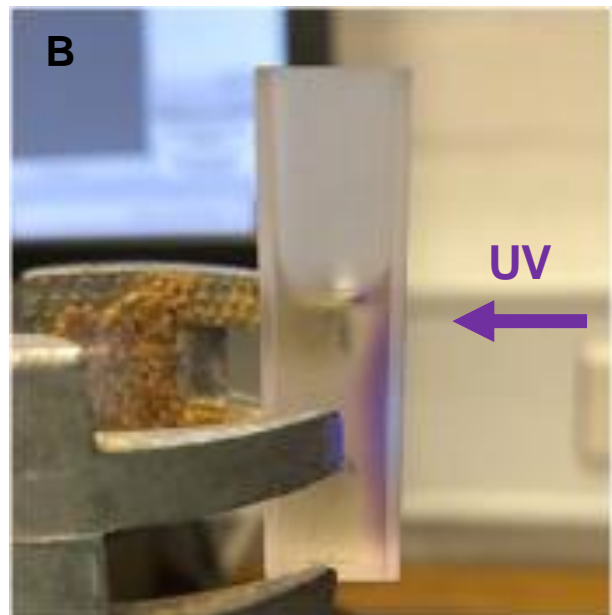
Supplementary Figure 21. Sensitivity of energy consumption for achieving unity equivalence ($W = 1$) to radial position. Results were obtained from numerical simulations. Each data point corresponds to a simulation of a voxel with a fixed radial position but randomized starting angle. Three levels of light extinction were tested: $\mu \cdot R = 50$ (black), 100 (blue) and 200 (red).



Supplementary Figure 22. Simulated effect of Species B-generation capacity on the efficiency of binary photoinhibition. The red line shows the nonlinear photoresponse required for a single-color tomographic printing system to function (only with Species A). Shaded area shows the duration of UV illumination (30 s). Visible light was always on. The capacity is measured as the maximum reachable concentration of Species B compared to the initial concentration of Species A. See Supplementary Movies 3-4 for a simulation in which $C_{B,max}/C_{A0} = 1$.



1 wt% *o*-Cl-HABI (M-1)



3 wt% *o*-Cl-HABI (M-3)

Supplementary Figure 23. Effect of *o*-Cl-HABI concentration on light extinction. The purple color indicates the depth to which UV light penetrated into the cuvette and stimulated lophyl radical generation via photolysis.

Supplementary Table 1-3

Component identifier in Fig. S1	Component
S1	Acer XD1270D
S2	Visitech VISITECH-LRS-4KA
S3	Thorlabs M625L4-C4
C1	XIMEA MQ042CG-CM
LP	Thorlabs FGL610S
A	Thorlabs SM1D12D
L1	optical lens $f = 200$ mm
L2	Thorlabs LA4984-UV
L3	Thorlabs LA4855-UV
L4	optical lens $f = 50$ mm
L5	optical lens $f = 200$ mm
L6	Thorlabs LA1353-A
L7	Thorlabs LA1255-A

Supplementary Table 1. Optomechanical components in the dual color tomographic vat photopolymerization assembly (Supplementary Fig. 1).

S1 (Visible)		S2 (UV)	
Line pair (cycles/mm)	Number of pixels (half-periods)	Line pair (cycles/mm)	Number of pixels (half-periods)
0.8	5	0.5	123
1.1	4	1	62
1.4	3	2	31
2.1	2	3.1	20
4.2	1	3.4	18
		4.1	15
		4.7	13
		6.2	10
		8.8	7
		12.3	5

Supplementary Table 2. Line pair settings in modulation transfer function (MTF) measurements

Workpiece	Confer	SC mode			DC mode		
		Visible exposure time (s)	Visible light dose (J)	Visible exposure time (s)	Visible light dose (J)	UV exposure time (s)	UV light dose (J)
Cuboid	Fig. 2e	48	0.034	-	-	-	-
Cuboid	Fig. 2e	52	0.037	52	0.037	52	0.75
Cuboid	Fig. 2e	56	0.041	56	0.041	56	0.80
Cuboid	Fig. 2e	60	0.043	60	0.043	60	0.85
Cuboid	Fig. 2e	66	0.047	66	0.047	66	0.93
Cuboid	Fig. 2e	72	0.052	72	0.052	72	1.0
Cuboid	Fig. 2e	-	-	78	0.056	78	1.1
Cuboid	Fig. 2e	-	-	84	0.06	84	1.2
Cuboid	Fig. 2f	16 + 29	0.053 + 0.021	16 + 29	0.053 + 0.021	23	0.10
Heart	Fig. 2i	46	0.073	48	0.077	30	0.90

Supplementary Table 3. Exposure times and estimated doses. All tests used Resin M-1.

Supplementary Movies

Supplementary Movie 1. Transient Stationary State. Evolution of phase diagram at constant illumination as a result of curing volume rotation. τ is the number of full rotations.

Supplementary Movie 2. DCTVP - species. Simulated printing process of an arbitrary geometry using dual color tomographic volumetric printing (DCTVP). Evolution of the states of two voxels with different fates.

Supplementary Movie 3. DCTVP - processes. Simulated printing process of an arbitrary geometry using dual color tomographic volumetric printing (DCTVP), with limited lophyl generation capacity accounted for.

Supplementary Movie 4. SCTVP - processes. Simulated printing process of an arbitrary geometry using single color tomographic volumetric printing (SCTVP).

Supplementary Movie 5. Simulated square printing. SC-1: with non-negativity constraint – negativities set to zero before projection; SC-2: with non-negativity constraint – negativities eliminated iteratively; DC: without non-negativity constraint – negativities projected using a second source of illumination. Color indicates extent of conversion (arb. unit).

Supplementary Movie 6. *In situ* imaging of cuboid printing. SC-1: single color printing. The process took 72 seconds using Resin M-1. DC: dual color printing. The process took 84 seconds using resin M-1. The framerate has been changed to shorten the clip. The diameter of the test tube is 11.3 mm.

Supplementary Movie 7. Time-dependent cross-section of the cuboids. SC: single color printing. DC: dual color printing. The brightness of pixels correlates with the inhomogeneity in refractive index stemming from polymerization. This clip was reconstructed from the footages presented in Video 6 using filtered back projection. The scale bars are 3.9 mm.

Supplementary Movie 8. *In situ* imaging of inverted pyramid printing. SC: single color printing of an inverted pyramid with a solid top plate. The process took 60 seconds using resin M-1. DC: dual color printing of an inverted pyramid. The polymerization of the top plate was arrested using UV, creating a flexible membrane that introduced the “parachute” effect during workpiece settling. The process took 66 seconds using resin M-1. The framerate has been changed to shorten the clip. The diameter of the test tube is 10 mm.

References

12. L. A. Feldkamp, L. C. Davis, J. W. Kress, Practical cone-beam algorithm. *Journal of the Optical Society of America A* **1**, 612-619 (1984).
13. M. Garland, P. S. Heckbert, Surface simplification using quadric error metrics. In *Proceedings of the 24th annual conference on Computer graphics and interactive techniques*. (1997), pp. 209-216.
14. A. Bærentzen, E. Rotenberg, Skeletonization via local separators. *ACM Trans. Graph.* **40**, 1-18 (2021).
15. C. Zhang, T. Chen, Efficient feature extraction for 2D/3D objects in mesh representation. In *Proceedings 2001 International Conference on Image Processing (Cat. No. 01CH37205)*. (IEEE, 2001), vol. 3, pp. 935-938.
16. A. Jacobson, L. Kavan, O. Sorkine-Hornung, Robust inside-outside segmentation using generalized winding numbers. *ACM Trans. Graph.* **32**, Article 33 (2013).
17. J. A. Bærentzen, J. Gravesen, F. Anton, H. Aanæs, in *Guide to computational geometry processing: Foundations, algorithms, and methods*, J. A. Bærentzen, J. Gravesen, F. Anton, H. Aanæs, Eds. (Springer London, London, 2012), pp. 263-275.
18. M. Schrödner, H. Schache, H. Lindauer, R. Schrödner, A. Konkin, Oscillations of the lophyl radical concentration during the photo-decomposition of o-cl-hexaarylbisimidazole. *Journal of Photochemistry and Photobiology A: Chemistry* **233**, 60-64 (2012).